Mode locking of hole spin coherences in $CsPb(Cl,Br)_3$ perovskite nanocrystals

E. Kirstein[1], N. E. Kopteva[1], D. R. Yakovlev[1,2,3], E. A. Zhukov[1,2], E. V. Kolobkova[4,5], M. S. Kuznetsova[6], V. V. Belykh[3], I. A. Yugova[6], M. M. Glazov[2], M. Bayer[1,2], and A. Greilich[1]

[1]*Experimentelle Physik 2, Technische Universität Dortmund, 44227 Dortmund, Germany*
[2]*Ioffe Institute, Russian Academy of Sciences, 194021 St. Petersburg, Russia*
[3]*P. N. Lebedev Physical Institute of the Russian Academy of Sciences, 119991 Moscow, Russia*
[4]*ITMO University, 199034 St. Petersburg, Russia*
[5]*St. Petersburg State Institute of Technology, 190013 St. Petersburg, Russia and*
[6]*Spin Optics Laboratory, St. Petersburg State University, 198504 St. Petersburg, Russia*

The spin physics of perovskite nanocrystals with confined electrons or holes is attracting increasing attention, both for fundamental studies and spintronic applications. Here, stable $CsPb(Cl_{0.5}Br_{0.5})_3$ lead halide perovskite nanocrystals embedded in a fluorophosphate glass matrix are studied by time-resolved optical spectroscopy to unravel the coherent spin dynamics of holes and their interaction with nuclear spins of the ^{207}Pb isotope. We demonstrate the spin mode locking effect provided by the synchronization of the Larmor precession of single hole spins in each nanocrystal in the ensemble that are excited periodically by a laser in an external magnetic field. The mode locking is enhanced by nuclei-induced frequency focusing. An ensemble spin dephasing time T_2^* of a nanosecond and a single hole spin coherence time of $T_2 = 13$ ns are measured. The developed theoretical model accounting for the mode locking and nuclear focusing for randomly oriented nanocrystals with perovskite band structure describes the experimental data very well.

Lead halide perovskite semiconductors are highly attractive due to their remarkable photovoltaic efficiency[1,2], and are promising for optoelectronic[3,4] and spintronic[4–7] applications. Perovskite nanocrystals (NCs) have recently extended the wide class of semiconductor NCs grown by colloidal synthesis[8–13]. They show a remarkable quantum yield of up to 90% even for bare NCs, as surface states do not act detrimentally on the exciton emission efficiency. For inorganic $CsPbX_3$ (X = I, Br, or Cl) NCs, the band gap can be tuned from the infrared up to the ultraviolet by mixing the halogen composition and by changing NC size, varying the quantum confinement of charge carriers. Additionally, the exciton fine structure can be adjusted by the NC shape[14–17].

In addition to the high quantum yield and tunable optical properties, the simple fabrication makes lead halide perovskite NCs interesting for applications. As far as spintronics is concerned, only quite a few studies have been performed so far. Neutral and charged excitons in single NCs were identified by their Zeeman splitting in magnetic field[18,19]. For NC ensembles, negatively charged excitons (trions) and dark excitons were identified in strong magnetic fields of 30 T[20]. Optical orientation, optical alignment and anisotropic exciton Zeeman splitting were observed[21]. The coherent spin dynamics of electrons and holes in $CsPbBr_3$ NCs[22,23] were explored, and the picosecond spin dynamics of carriers in $CsPbI_3$ NCs were reported[24]. Despite the progress in crystal growth, perovskite NCs still suffer from insufficient long-term stability of optical properties. A promising approach here is to synthesize NCs embedded in glass, providing protection by encapsulation[25,26].

As a result, perovskite NCs in a glass matrix may be suitable for quantum technologies. For reference, one may compare NCs with the established system of self-assembled (In,Ga)As/GaAs quantum dots (QDs) singly charged with an electron or a hole. Using all-optical approaches one can orient and manipulate the spins of the charge carriers on the picosecond timescale at high operation frequencies[30,31]. There are two complementary concepts: the first one uses a single spin in a QD for establishing a quantum bit, the second one exploits a QD ensemble which may be suited for a quantum memory with sufficiently strong light-matter interaction. Here we focus on a NC ensemble, which gives information on the average spin properties and their scatter due to inhomogeneity. The inhomogeneity obstacle, however, can be overcome by applying periodic laser excitation that synchronizes the electron spin Larmor precession in different NCs subject to a transverse magnetic field. This spin mode locking (SML) effect, initially discovered in singly charged (In,Ga)As QDs, allows one to uncover the spin coherence of individual carriers, which is typically prevented due to the faster spin dephasing in the ensemble[32–34]. The interaction of resident carrier spins with the surrounding nuclear bath provides further flexibility with potential memory times up to hours and exchange interaction fields up to a few Tesla[35,36]. This collective phenomenon of spin dynamics homogenization has been demonstrated so far only for (In,Ga)As QDs.

In this paper we demonstrate the SML effect for holes in a totally different class of QDs, namely perovskite $CsPb(Cl_{0.5}Br_{0.5})_3$ NCs synthesized in a glass matrix. We provide detailed information on the spin dynamics of confined holes correlated with the appearance of spin mode locking. We measure the g-factor, spread of g-factors, longitudinal spin relaxation time T_1, transversal spin coherence time T_2, and inhomogeneous spin dephasing time T_2^*. Exploiting the hyperfine interaction with the nuclear spins, we implement dynamic nuclear polariza-

tion and optically-detected nuclear magnetic resonance (ODNMR) to identify the involved nuclear isotopes. A theoretical model of the SML in the perovskite is developed to account for the inverted band structure and for the dominating role of the hole-nuclear interaction, compared to self-assembled QDs. As an additional challenge, the random orientation of NCs in the ensemble is considered.

RESULTS

The optical properties of $CsPb(Cl_{0.5}Br_{0.5})_3$ nanocrystals embedded in a fluorophosphate glass are shown in Fig. 1a. At cryogenic temperature of $T = 5$ K the transmission spectrum of the NCs with about 7 nm size shows pronounced exciton resonance at 2.743 eV, which is broadened due to NC size dispersion. The exciton resonance can be also traced by the spectral dependence of the time-resolved Faraday ellipticity (TRFE) amplitude. The exciton population dynamics is measured by time-resolved differential transmission ($\Delta T/T$), showing a decay time of 160 ps, which corresponds to the exciton lifetime (inset in Fig. 1a).

To study the coherent spin dynamics of resident carriers we use the pump-probe technique with spin-sensitive detection of the Faraday ellipticity, whose potential has been approved for lead halide perovskite crystals[38–40], polycrystalline films[23,41,42], and $CsPbBr_3$ NCs[22,23]. The pump laser pulses are circularly polarized and, according to the selection rules, generate spin polarization of electrons and holes along the light $\mathbf{k}$ vector. The oriented carrier spins precess at the Larmor frequency around the magnetic field applied in the Voigt geometry B_V ($\mathbf{B} \perp \mathbf{k}$). The coherent spin dynamics is then detected through the Faraday ellipticity of the linearly-polarized probe pulses.

A typical TRFE signal, measured at $T = 1.6$ K in $B_V = 1$ T, is shown in the upper part of Fig. 1b. It shows oscillations with the Larmor frequency ω_L which is a linear function of B_V: $\omega_L = |g|\mu_B B_V/\hbar$. This allows us to evaluate the g-factor of $|g| = 1.20$. ω_L has no offset at zero magnetic field (Fig. S4a), which is a strong argument in favor of the presence of resident carriers in the NCs rather than of carriers bound in an exciton[23]. In the latter case, an offset equal to the electron-hole exchange would be expected. General theoretical arguments and the experiments on dynamic nuclear polarization (Fig. 2c, see details below) indicate that the g-factor has a positive sign. From its value and the strong changes of ω_L in presence of polarized nuclei we conclude that the signal is dominated by resident holes with $g_h = +1.20$ (see Supplementary Notes S1 and S2). Note, that the stronger hole-nuclear interaction compared to the electron-nuclear one is specific for lead halide perovskite semiconductors[39], due to their "inverted" band structure in comparison to semiconductors like GaAs or CdTe.

The TRFE amplitude decays within a nanosecond due to spin dephasing in the ensemble of NCs showing a dispersion of Larmor frequencies. The spin dephasing time at $B_V = 1$ T is $T_2^* = 0.26$ ns, and it increases up to 0.5 ns at low magnetic fields. There it becomes limited by the hole interaction with the nuclear spin fluctuations. In stronger fields, T_2^* decreases as $1/B_V$ due to the g_h dispersion $\Delta g = 0.03$ (Fig. S4b). By using the spin inertia technique[43] we measured the longitudinal spin relaxation time $T_1 = 7.6\,\mu$s in zero longitudinal magnetic field, which gives an estimate of the upper limit of T_2 in the studied NCs (Supplementary Note S4).

Spin mode locking in nanocrystal ensemble

The most striking feature of the TRFE signal (blue) in Fig. 1b is the presence of oscillating signal at negative time delays, before the pump. Its amplitude has a maximum at small negative delays and decays with increasing negative delay with the same dephasing time as at positive delays. For such a signal to occur, optically-induced spin coherence should be present in the NCs for times exceeding the repetition period of the laser pulses $T_R = 13.2$ ns, and can therefore be obtained for spin coherence times $T_2 \geq T_R$. The same effect was observed in ensembles of singly charged (In,Ga)As/GaAs QDs with both negative and positive charging[32,34,44]. It is caused by synchronization of the Larmor spin precession in the ensemble of NC carriers with the periodic laser pumping, termed the spin mode locking effect[37].

The SML effect results from the efficient accumulation of spin polarization from carrier spins which Larmor frequencies ω_L are commensurate with the laser repetition period T_R. These spin precession modes fulfill the phase synchronization condition (PSC): $\omega_L = N\omega_R = 2\pi N/T_R$, with N being an integer. If the single spin coherence time exceeds T_R, the spin polarization of these modes accumulates. Modes fulfilling the PSC are shown schematically in Fig. 1c, assuming a Gaussian distribution of the Larmor frequencies centered around $N = 3$ for the weight of their contribution, as shown Fig. 1d by the green line with the spread of Larmor frequencies $\Delta\omega$. $\Delta\omega$ is contributed by the g-factor dispersion and by the nuclear spin fluctuations (Supplementary Note S4). Inside this distribution, the five essential PSC modes (red needles) are located.

The signal resulting from the sum of the five PSC modes is shown at the bottom of Fig. 1c. The maxima of the PSC mode signal coincide with the pump pulse arrival times, in between the signal is reduced with a symmetry relative to the center between the pump pulses: the ensemble spin polarization dephases after a pump pulse, but then revives before the next pump. The pump pulse excites each time all modes within the Gaussian distribution, but only the PSC modes are amplified from pulse to pulse and contribute to the SML signal at negative delays. Remarkably, the spin coherence time T_2 of the holes in individual NCs can be determined from the ratio of the

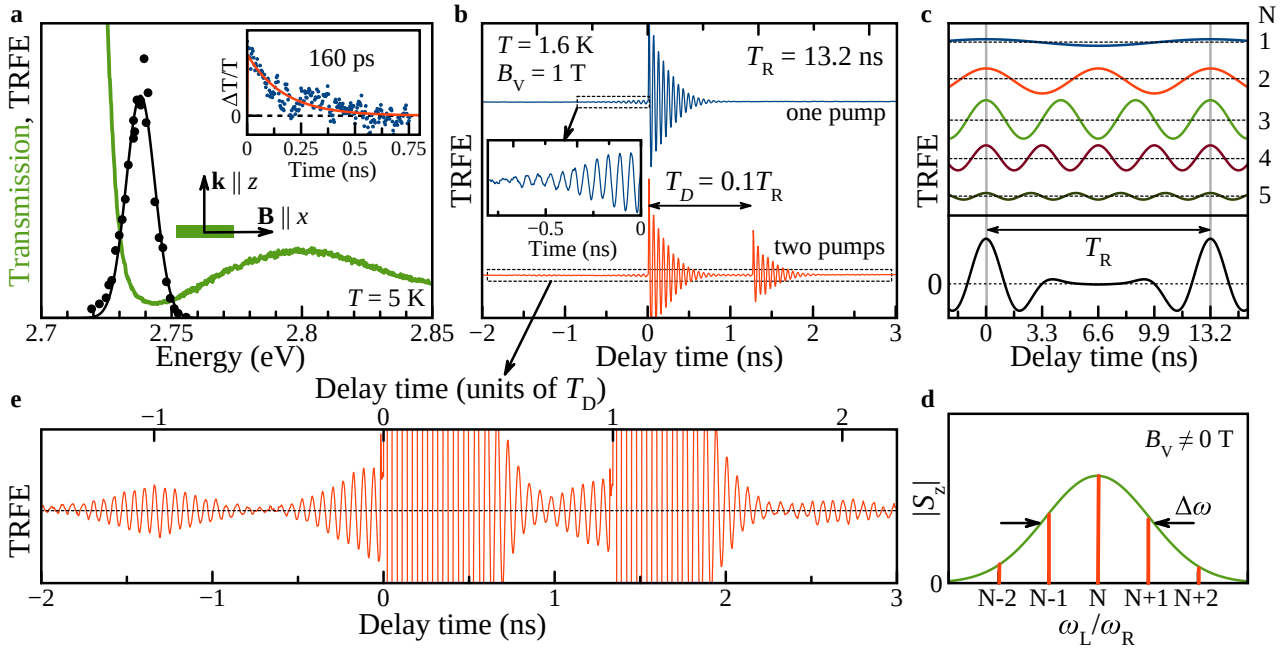

FIG. 1. **Spin mode locking in CsPb(Cl,Br)$_3$ NCs.** **a**, Transmission spectrum of $CsPb(Cl_{0.5}Br_{0.5})_3$ NCs (green line). Black dots show spectral profile of the Faraday ellipticity amplitude measured at zero pump-probe time delay fitted by a Gaussian function (black line). $T = 5$ K. Inset shows time-resolved differential transmission (dots) with a monoexponential fit (red line) providing the exciton lifetime of 160 ps. **b**, Time-resolved Faraday ellipticity (TRFE) measured at the photon energy of 2.737 eV with 1.5 ps laser pulses. Blue curve shows data for the one-pump protocol with a repetition period of $T_R = 13.2$ ns using the pump power $P_{pu} = 25$ mW. Inset shows zoom of signal before the arrival of the pump pulse, indicated by the box. Red curve is TRFE for the two-pump protocol ($T_D = 0.1T_R = 1.32$ ns) using the pump powers $P_{pu,1} = 25$ mW and $P_{pu,2} = 13$ mW. $T = 1.6$ K and $B_V = 1$ T. **c**, Scheme shows spins precessing at five lowest PSC mode frequencies. Black curve at the bottom shows sum signal of these modes, each weightes assuming an ensemble with a Gaussian distribution of amplitudes, as shown in panel d by the red vertical lines. **d**, Illustration of the pumped carrier spin polarizations in inhomogeneous NC ensemble subject to a magnetic field. Green line shows the distribution of carrier precession frequencies caused by dispersion of the Larmor frequency. It is modeled by Gaussian with width $\Delta\omega$. PSC modes for the one-pump protocol, fulfilling the condition $\omega_L = N\omega_R = 2\pi N/T_R$, are shown by the red vertical lines. **e**, Zoom of the TRFE signal in the two-pumps protocol from panel b, indicated by the box. Upper scale gives delay in units of separation, T_D, between two pumps. The bursts in the signal are associated with the electron spins with Larmor frequencies that are commensurate with the frequency: $\omega_D = 2\pi M/T_D$.

signal amplitudes at negative and positive delays. This requires a modeling approach, that we will present in the following.

It was shown for (In,Ga)As QDs that the spectrum of PSC modes and the shape of TRFE signal can be tailored by using a two-pump protocol, where an additional second pump pulse is applied with a time delay T_D with respect to the first pump pulse. In this case, an additional synchronization condition is introduced, as the amplified PSC modes have to satisfy two commensurability conditions: $\omega_L = 2\pi N/T_R$ and $\omega_L = 2\pi M/T_D$, with M being an integer[32,34]. In the experiment this leads to the emergence of signal bursts at multiple times of T_D. This behaviour is indeed also found in the studied perovskite NCs, as one can see from the red colored signal in Fig. 1b and its zoom in Fig. 1e, measured with $T_D = 0.1\,T_R = 1.32$ ns. Two bursts at -1.32 ns and $+2.64$ ns are seen very prominently. A scheme of the PSC mode spectrum modification for the two-pump case is given in Fig. 2b.

Nuclei-induced frequency focusing

In semiconductors, the spin dynamics of electrons and holes are strongly influenced by their interaction with the nuclear spin system in which they are embedded[45]. Polarized nuclei provide the Overhauser field B_N, which shifts the carrier Larmor precession frequency to $\omega_L = |g|\mu_B(B_V + B_N)/\hbar$. Thereby, spin precession modes in Fig. 1d, that do not match the PSC, can be shifted in their frequency such that they satisfy the PSC. This effect was found experimentally in (In,Ga)As QDs and identified as nuclei-induced frequency focusing (NIFF) of the carrier spin coherence[33]. The NIFF mechanism represents a positive feedback loop, that provides the required nuclear polarization in each QD, so that a large dot fraction in the ensemble is pushed into PSC modes. Due to the very slow nuclear spin relaxation at cryogenic tem-

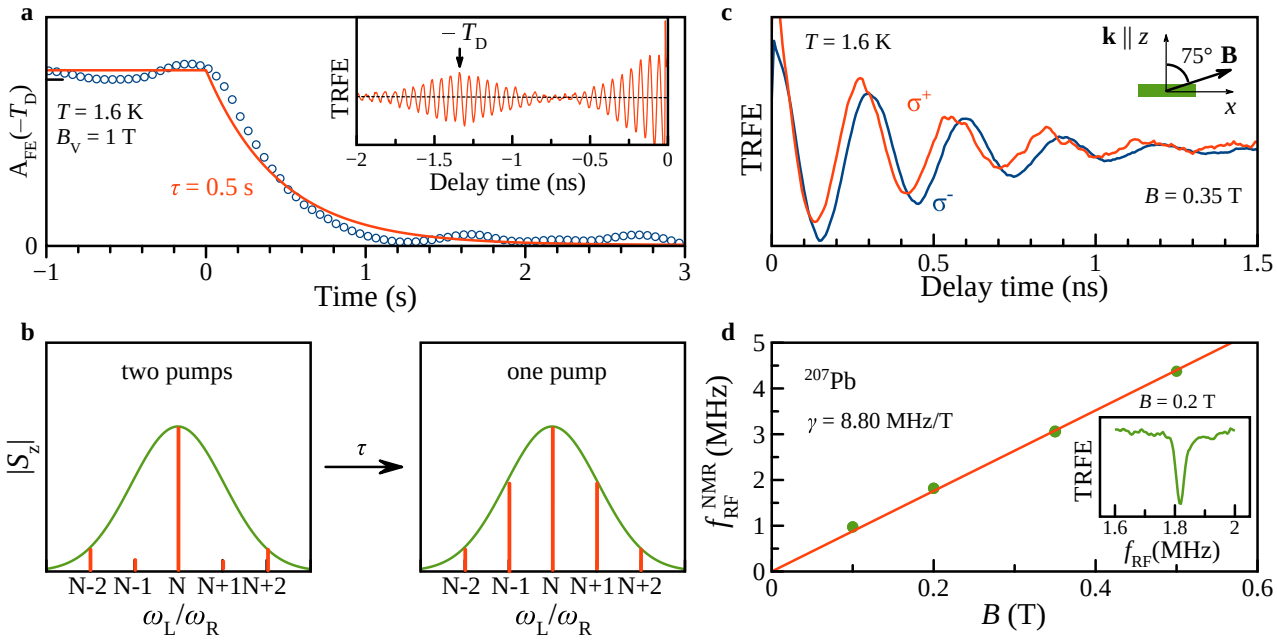

FIG. 2. **Hole-nuclei hyperfine interaction.** **a**, Relaxation dynamics of the burst amplitude $A_{\rm FE}(-T_{\rm D})$ measured by switching from two-pump to one-pump protocol. $T = 1.6\,$K and $B_{\rm V} = 1\,$T. Exponential fit gives decay time of the burst amplitude $\tau = 0.5\,$s, corresponding to the changeover time between the distributions, after blocking the second pump. Inset shows TRFE for negative time delays in the two-pump protocol. Arrow at delay of $-T_{\rm D} = -1.32\,$ns marks the position of the amplitude relaxation measurement. **b**, Schematic representation of the distribution $|S_z|$ of spin precession modes within the g-factor spread (green Gaussian) in the two-pump compared to the one-pump protocol. **c**, TRFE signal for two circular polarizations of pump: σ^+ (red) and σ^- (blue). Magnetic field $B = 0.35\,$T is tilted from the light propagation direction by the angle $\alpha = 75°$. **d**, Magnetic field dependence of ODNMR frequency (dots). Line is a linear fit with slope matching the gyromagnetic ratio $\gamma = 8.8\,$MHz/T of ^{207}Pb. Inset shows typical resonance curve at $B = 0.2\,$T.

peratures, the NIFF configuration can be kept for hours.

In an ideal, very efficient, system as is the case for (In,Ga)As QDs with strong carrier-nuclei interaction, NIFF results in identical amplitudes of the TRFE signal at negative and positive time delays, meaning that all precession frequencies are focused on the PSC modes. This is obviously not the case for the studied perovskite NCs, see Fig. 1b. Still, NIFF is present as can be evidenced by the relaxation dynamics of the bunch amplitude at $-1.32\,$ns delay when the second pump is blocked[33]. In Fig. 2a we demonstrate such a measurement. We find the decay time of $\tau = 0.5\,$s, which is related to the repolarization of the nuclear spin system from the two-pump to the one-pump protocol, sketched in Fig. 2b. Without nuclear involvement the amplitude of the signal would decay within the carrier spin coherence time T_2 after switching off the second pump, as was the case for hole spins in (In,Ga)As QDs[44].

Dynamic nuclear polarization and ODNMR

To further justify the involvement of nuclear spins, we apply the method of dynamic nuclear polarization (DNP) in a titled magnetic field[46]. The spin polarization of optically-oriented carriers is transferred via the hyperfine interaction to the nuclear spin system. The Overhauser field of the polarized nuclei $\mathbf{B}_{\rm N}$ acts back on the carriers and shifts their Larmor precession frequency, the detailed scheme can be found in Supplementary Note S2 and Ref.[39]. The shift of the Larmor frequency allows one to measure the nuclear spin polarization.

One can see in Fig. 2c, that for σ^+ pump the Larmor precession becomes faster compared to the σ^- case. The relative frequency shift is considerable, which is typical for the strong hole-nuclei spin interaction in perovskites. It allows us to confirm that the TRFE signal is related to holes and to evaluate the Overhauser field of $B_{\rm N} = 5.8\,$mT. The sign of the observed Larmor frequency change corresponds to a positive hole g-factor.

The variation of the TRFE signals by the DNP effect allows us to use it for optical detection of nuclear magnetic resonance (ODNMR)[39]. For that, the time delay is fixed and the TRFE amplitude is measured as a function of the radio frequency of additional radiation with $f_{\rm RF} = 0.1 - 10\,$MHz. The nuclear spin system is depolarized when the energy $hf_{\rm RF}$ matches to Zeeman splitting of a nuclear isotope $\mu_{\rm N} g_{\rm N} B$, i.e. for a NMR. Here, $\mu_{\rm N}$ is the nuclear magneton and $g_{\rm N}$ is the nuclear g-factor (Supplementary Table S1). In the experiment it is de-

tected as a resonant decrease of the TRFE amplitude, as shown in the insert of Fig. 2d at $B = 0.2$ T. From a linear fit of the resonance frequency dependence on the magnetic field $f_{\rm RF}^{\rm NMR}(B)$, we evaluate the gyromagnetic ratio $\gamma = \mu_{\rm N} g_{\rm N}/\hbar = 8.8$ MHz/T, see Fig. 2d. One can conclude from the Supplementary Table S1 that among the nuclear isotopes present in the $CsPb(Cl,Br)_3$ NCs only the ^{207}Pb isotope matches this value. The dominant role of ^{207}Pb on the carrier spin dynamics was identified earlier in $FA_{0.9}Cs_{0.1}PbI_{2.8}Br_{0.2}$ crystals and the theoretical analysis establishes it as common feature for lead halide perovskites[39].

Theory of spin mode locking in perovskite NCs

The theory of spin mode locking was previously developed for self-assembled quantum dots[47] and successfully applied to explain experimental results[37,44,48]. However, the discovery of SML in perovskite nanocrystals provide new theoretical challenges. First, the generation of spin coherence in perovskite structures with an inverted band structure occurs on the basis of other selection rules[45]. Circularly polarized light generates an exciton with an electron and a hole, both having spin 1/2, instead of an exciton with an electron (1/2) and a heavy hole (3/2). Second, perovskite colloidal nanocrystals in ensemble are randomly oriented. For a complete theoretical description, the anisotropy of the g-factor for a single NC and the possibility of generating spin coherence through positively and negatively charged trions have to be considered. Taking all these facts into account requires a significant adjustment of the theoretical model.

The model, which details are given in Supplementary Notes S6-S10, has two key parts: the first one considers the spin coherence generation and its dynamics in magnetic field for a single nanocrystal with arbitrary oriented crystallographic axes. The second part accounts for inhomogeneity of the NC ensemble, namely the NCs random orientation and the g-factors spread.

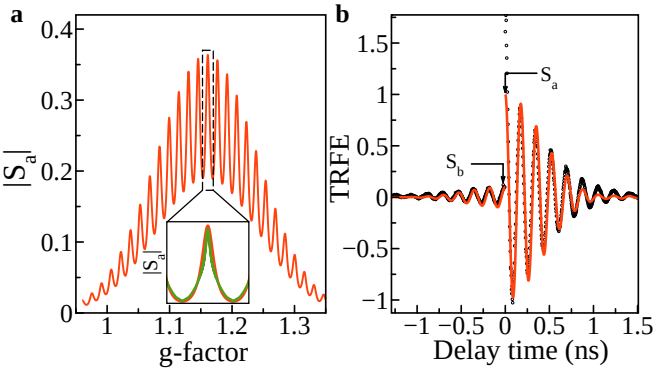

FIG. 3. **Calculation of spin polarization and TRFE signal. a**, Spectral distribution of precessing modes for $T_2 = 28$ ns. Inset: illustration of precessing mode with NIFF for $T_2 = 13$ ns (green) and without NIFF for $T_2 = 28$ ns (red). **b**, Time-resolved Faraday ellipticity (dots) measured at $B_{\rm V} = 0.35$ T and its modeling (red line).

Without loss of generality we consider resident holes, that can be created by photo-charging, as in experiment the SML of holes is observed. The resident carrier spin polarization, providing the pump-probe signal, is generated by a mechanism involving trions. The oriented spin polarization components are tilted relative to the direction of the magnetic field, precess about it in time, and decay with the spin coherence time T_2. For $T_2 \geq T_R$ the spin polarization accumulates by pumping with a train of optical pulses. The SML is an ensemble effect resulting from a large number of oscillating signals with frequencies commensurate with T_R, therefore, the model takes into account the spread of the g-factors (Supplementary Note S8).

Experimental spin dynamics measured at $B_{\rm V} = 0.35$ T (black dots in Fig. 3b) is modeled numerically using Supplementary Eqs. (S28-S61). The signal decay at negative and positive time delays is described by the T_2^* that is given by the g factor spread, Δg, and nuclear spin fluctuations, $\delta B_{\rm N}$. The ratio S_b/S_a of amplitudes before pulse arrival S_b and after pulse arrival S_a is determined by T_2, the optical pulse area Θ and the NIFF effect. Technically, we calculate the spin polarization distribution S_a as a function of the Larmor frequency parametrized by the hole g factor $\omega_{\rm L} = g_h \mu_B B_V/\hbar$ (Fig. 3a). The distribution width is defined by $2\Delta g$ with $\Delta g = 0.06$. The multiple peaks correspond to the synchronized precession modes with the width of each peak determined by $1/T_2 + 1/\mathcal{T}_2^*$, where $\mathcal{T}_2^* \sim \hbar/(g_h \mu_B \sqrt{\delta B_{\rm N}^2})$ is related to the nuclear spin fluctuations. The modeled SML signal corresponding to the distribution is shown by red line in Fig. 3b. It reproduces well all features of the experimental data.

In order to highlight the role of hole-nuclei interaction for the measured SML we perform modeling without and with account for NIFF. Without NIFF we get the hole spin coherence time $T_2 = 28$ ns for $\Theta = \pi$ as the best fit parameters. The nuclear polarization changes the spin polarization distribution by increasing $\mathcal{T}_2^*$ and narrowing precession modes. This results in increase of the ratio S_b/S_a and to match its experimental value of 0.1 the shorter spin coherence time should be taken to keep the mode width same (insert of Fig. 3a). With NIFF we get $T_2 = 13$ ns, which is at the lower limit of the times required for SML to occur. It is remarkable that due to the involvement of NIFF we are able to observe the SML effect for such a short-lived hole spin coherence.

Conclusions

We have demonstrated the outstanding potential of perovskite NCs embedded in a glass matrix, using their spin properties as exemplary feature. We find a very long hole spin lifetime up to the microsecond range. We

present an additional class of materials, in which the effects of spin mode locking and nuclei-induced frequency focusing are observed. This allows one to measure the hole spin coherence time T_2, disregarding the random NC orientation and variation of NC sizes and shapes. It opens the pathway for implementation of multi-pulse protocols for manipulating the spin coherence, also with involvement of strong hole-nuclei interaction provided by the inverted band structure of the lead halide perovskites. The choice of glass matrix or NC synthesis does not limit the observed effects fundamentally. We are convinced that they can be observed in many different lead halide perovskite NCs, but also in lead-free NCs.

METHODS

Samples. The studied $CsPb(Cl,Br)_3$ nanocrystals embedded in fluorophosphate $Ba(PO_3)_2$ glass were synthesized by rapid cooling of a glass melt enriched with the components needed for the perovskite crystallization. Samples of fluorophosphates (FP) glasses of $60Ba(PO_3)_2 - 15NaPO_3 - 12AlF_3 - 1Ga_2O_3 - 4Cs_2O - 8PbF_2$ (mol. %) composition doped with 16 mol.% NaCl, 3.4 mol.% $BaBr_2$ were prepared using the melt-quench technique. The glass synthesis was performed in a closed glassy carbon crucible at temperatures of 1000-1050°C. About 50 g of the mixed powder was melted in the crucible during 20 min. Then the glass melt was cast on a glassy carbon plate and pressed to form a plate with the thickness of about 2 mm. The formation of the crystalline phase in glass can be carried out directly in the process of cooling the melt. During the pouring out of the transparent melt spontaneous precipitation of NCs with sizes smaller than the Bohr exciton radius occurs. By a subsequent heat treatment at a temperature just above the glass transition temperature ($400 - 429$°C), it is possible to sequentially grow NCs to large sizes. The details of the method are given in Ref.[26].

The NC size of 7 ± 1 nm is evaluated from XRD data. The composition of the $CsPb(Cl_{0.5}Br_{0.5})_3$ NCs is estimated from the energy of the transmission edge (Fig. 1a). At $T = 5$ K the exciton resonance broadened due to NC size dispersion is at 2.743 eV. The band gap lies between that of bulk $CsPbBr_3$ and bulk $CsPbCl_3$. The optical transition is shifted by about 90 meV due to quantum confinement[29,49]. For optical experiments, the sample with thickness of 500 μm was polished from both sides. The remarkable advantage of NCs in a glass matrix versus wet-chemistry synthesized NCs is the encapsulation resulting in long-term stability. Also the possibility to have optically flat sample surfaces with diminished light scattering is important for the polarization sensitive optical techniques used in this study.

Magneto-optical measurements. For low-temperature optical measurements we use a liquid helium cryostat with temperature variable from 1.6 K up to 300 K. At $T = 1.6$ K the sample is immersed in superfluid helium, while at $4.2 - 300$ K it is held in helium gas. A superconducting vector magnet equipped with three orthogonal pairs of split coils to orient the magnetic field up to 3 T along any arbitrary direction is used. The magnetic field parallel to $\mathbf{k}$ is denoted as B_F (Faraday geometry), perpendicular to $\mathbf{k}$ as B_V (Voigt geometry). If not stated otherwise, the B_V is oriented horizontally. The angle α is defined as the angle between $\mathbf{B}$ and the light wave vector $\mathbf{k}$, where $\alpha = 0°$ corresponds to $\mathbf{B}_\mathrm{F}$.

Transmission spectra. For measuring of the optical transmission a white light halogen lamp is used. The sample was thinned to 43 μm in order to avoid saturation of light absorption in the spectral range of exciton resonances. The spectra are detected by a 0.5 m monochromator equipped with a silicon charge-coupled-device camera.

Time-resolved Faraday ellipticity (TRFE). The coherent spin dynamics are measured using a degenerate pump-probe setup[34]. A titanium-sapphire (Ti:Sa) laser generates 1.5 ps long pulses in the spectral range of $700 - 980$ nm ($1.265 - 1.771$ eV), which are frequency doubled with a beta barium borate crystal to the range of $350 - 490$ nm ($2.530 - 3.542$ eV). The laser spectral width is about 1 nm (about 2 meV), and the pulse repetition rate is 76 MHz (repetition period $T_\mathrm{R} = 13.2$ ns). The laser output is split into two beams, pump and probe, which pulses can delayed with respect to one another by a mechanical delay line. The laser photon energy is tuned to be in resonance with the exciton transition, e.g. at 2.737 eV at $T = 1.6$ and 5 K. The pump and probe beams are modulated using photo-elastic modulators (PEM). The probe beam is linearly polarized and its amplitude is modulated at 84 kHz, while the pump beam is either helicity modulated at 50 kHz between σ^+/σ^- circular polarizations or amplitude modulated at 100 kHz with the circular polarization fixed at either σ^+ or σ^-. Signal was measured by lock-in amplifier at difference frequency of the pump and probe modulation. For measuring by spin inertia technique, the modulation frequency of the pump helicity f_m was varied from 1 kHz to 5 MHz by an electro-optical modulator (EOM). For measuring the spin dynamics induced by the pump pulses, the polarization of the transmitted probe beam was analyzed with respect to its ellipticity (Faraday ellipticity) using balanced photodiodes and a lock-in amplifier. In $B_\mathrm{V} \neq 0$, the Faraday ellipticity amplitude oscillates in time reflecting the Larmor precession of the charge carrier spins. The dynamics of the Faraday ellipticity signal can be described by a decaying oscillatory function:

$$A_\mathrm{FE}(t) = S \cos(\omega_\mathrm{L} t) \exp(-t/T_2^*). \quad (1)$$

Here S is the amplitude at zero delay, ω_L is the Larmor precession frequency, and T_2^* the spin dephasing time. For application of a two-pump pulse scheme, after the delay line the so far not modulated linearly polarized pump beam was passed through a 50/50 nonpolarizing beam splitter. The deflected beam was sent via two mirrors over a certain distance and merged with the transmit-

ted pump beam via a second nonpolarizing 50/50 beam splitter. By careful adjustment both pump beams were brought aligned parallel to each other, to excite the same sample spot.

Pump-probe time-resolved differential transmission. Here, for excitation by the pump beam, the same scheme as in TRFE is used, but with linear polarization. The pump is amplitude modulated by a photoelastic modulator at 100 kHz. The linearly polarized, unmodulated probe beam is separated into a reference beam, which is routed around the cryostat and the test beam, which is transmitted through the sample. The signal is recorded with respect to the intensity difference between the transmitted and the reference beams, using a balanced photodetector.

Optically-detected nuclear magnetic resonance (ODNMR) with TRFE detection. In this technique nuclear magnetic resonances are measured via resonant decrease of dynamical nuclear polarization by radio frequency (RF) radiation. For that optical detection of the TRFE amplitude at fixed magnetic field is used. A small RF coil of about 5 mm diameter having 5 turns is placed close to the sample surface, similar to Ref.[50]. The coil is mounted flat at the sample surface and the laser beam is transmitted through the bore of the coil. The RF induced magnetic field direction is perpendicular to its surface and parallel to **k**. The RF in the frequency range f_{RF} from 100 Hz up to 10 MHz is driven by a frequency generator, with an applied voltage of 10 V leading to an oscillating field amplitude of about 0.1 mT. The RF is terminated by internal 50Ω resistors, but not frequency matched to the circuit. In the low frequency range up to 5 MHz the current is nearly frequency independent, as the inductive resistance of the coil is small compared to the internal termination. For observation of DNP it is essential to tilt the external magnetic field away from the Voigt geometry, to have a nonzero scalar product $\mathbf{B} \cdot \mathbf{S}$ and apply a constant pump helicity.

Acknowledgements

The authors are thankful to Al. L. Efros, M. A. Semina, and M. O. Nestoklon for fruitful discussions. We thank M. L. Skorikov for help with experiment. We acknowledge financial support by the Deutsche Forschungsgemeinschaft via the SPP2196 Priority Program (Project YA 65/26-1) and the International Collaborative Research Centre TRR160 (Projects A1 and B2). M.M.G. acknowledges support of the Russian Foundation for Basic Research (Grant No. 19-52-12038). The low-temperature sample characterization was partially supported by the Ministry of Science and Higher Education of the Russian Federation (Contract No. 075-15-2021-598 at the P. N. Lebedev Physical Institute). M.S.K. and I.A.Yu. acknowledge the Saint-Petersburg State University (Grant No. 91182694) and the Russian Foundation for Basic Research (RFBR Project No. 19-52-12059). Synthesis of the samples have been supported by Priority 2030 Federal Academic Leadership Program.

1. Jena, A. K., Kulkarni, A. and Miyasaka, T. Halide perovskite photovoltaics: Background, status, and future prospects. *Chemical Reviews* **5**, 3036–3103 (2019).
2. Best Research - Cell Efficiency Chart, `https://www.nrel.gov/pv/cell-efficiency.html` (2021).
3. *Halide Perovskites for Photonics*, eds. Vinattieri, A. and Giorgi, G. (AIP Publishing, Melville, New York, 2021).
4. *Hybrid Organic Inorganic Perovskites: Physical Properties and Applications*, eds. Vardeny, Z. V. and Beard, M. C. (World Scientific, 2022).
5. Wang, J., Zhang, C., Liu, H., McLaughlin, R., Zhai, Y., Vardeny, S. R., Liu, X., McGill, S., Semenov, D., Guo, H., Tsuchikawa, R., Deshpande, V. V., Sun, D. and Vardeny, Z. V. Spin-optoelectronic devices based on hybrid organic-inorganic trihalide perovskites. *Nat. Commun.* **10**, 129 (2019).
6. Ning, W., Bao, J., Puttisong, Y., Moro, F., Kobera, L., Shimono, S., Wang, L., Ji, F., Cuartero, M., Kawaguchi, S., Abbrent, S., Ishibashi, H., De Marco, R., Bouianova, I. A., Crespo, G. A., Kubota, Y., Brus, J., Chung, D. Y., Sun, L., Chen, W. M., Kanatzidis, M. G. and Gao, F. Magnetizing lead free halide double perovskites. *Science Advances* **6**, eabb5381 (2020).
7. Kim, Y.-H., Zhai, Y., Lu, H., Pan, X., Xiao, C., Gaulding, E. A., Harvey, S. P., Berry, J. J., Vardeny, Z. V., Luther, J. M. and Beard, M. C. Chiral-induced spin selectivity enables a room-temperature spin light-emitting diode. *Science* **371**, 1129 (2021).
8. Kovalenko, M. V., Protesescu, L. and Bondarchuk, M. I. Properties and potential optoelectronic applications of lead halide perovskite nanocrystals. *Science* **358**, 745–750 (2017).
9. Chen, Q., Wu, J., Ou, X., Huang, B., Almutlaq, J., Zhumekenov, A. A., Guan, X., Han, S.; Liang, L., Yi, Z., Li, J., Xie, X., Wang, Y., Li, Y., Fan, D., Teh, D. B. L., All, A. H., Mohammed, O. F., Bakr, O. M., Wu, T., Bettinelli, M., Yang, H., Huang, W., and Liu, X. All-inorganic perovskite nanocrystal scintillators. *Nature* **561**, 88–93 (2018).
10. Protesescu, L., Yakunin, S., Bodnarchuk, M. I., Krieg, F., Caputo, R., Hendon, C. H., Yang, R. X., Walsh, A. and Kovalenko, M. V. Nanocrystals of cesium lead halide perovskites ($CsPbX_3$, X = Cl, Br, and I): Novel optoelectronic materials showing bright emission with wide color gamut. *Nano Lett.* **15**, 3692–3696 (2015).
11. Akkerman, Q. A., Rainó, G., Kovalenko, M. V. and Manna, L. Genesis, challenges and opportunities for colloidal lead halide perovskite nanocrystals. *Nature Mater.* **17**, 394 (2018).
12. Park, Y.-S., Guo, S., Makarov, N. S. and Klimov, V. I. Room temperature single-photon emission from individual perovskite quantum dots. *ACS Nano* **9**, 10386–10393

(2015).
13. Yu, B., Zhang, C., Chen, L., Qin, Z., Huang, X., Wang X. and Xiao M. Ultrafast dynamics of photoexcited carriers in perovskite semiconductor nanocrystals. *Nanophotonics* **10**, 1943–1965 (2021).
14. Becker, M. A., Vaxenburg, R., Nedelcu, G., Sercel, P. C., Shabaev, A., Mehl, M. J., Michopoulos, J. G., Lambrakos, S. G., Bernstein, N., Lyons, J. L., Stöferle, T., Mahrt, R. F., Kovalenko, M. V., Norris, D. J., Rainó, G., and Efros, A. L. Bright triplet excitons in caesium lead halide perovskites. *Nature* **553**, 189 (2018).
15. Lin, J., Gomez, L., de Weerd, C., Fujiwara, Y., Gregorkiewicz, T. and Suenaga, K. Direct observation of band structure modifications in nanocrystals of $CsPbBr_3$ perovskite. *Nano Lett.* **16**, 7198 (2016).
16. Tamarat, Ph., Bodnarchuk, M. I., Trebbia, J.-B., Erni, R., Kovalenko, M. V., Even, J. and Lounis, B. The ground exciton state of formamidinium lead bromide perovskite nanocrystals is a singlet dark state. *Nature Mater.* **18**, 717–724 (2019).
17. Ramade, J., Andriambariarijaona, L. M., Steinmetz, V., Goubet, N., Legrand, L., Barisien, T., Bernardot, F., Testelin, C., Lhuillier, E., Bramati, A., and Chamarro, M. Fine structure of excitons and electron-hole exchange energy in polymorphic $CsPbBr_3$ single nanocrystals. *Nanoscale* **10**, 6393–6401 (2018).
18. Fu, M., Tamarat, P., Huang, H., Even, J., Rogach, A. L. and Lounis, B. Neutral and charged exciton fine structure in single lead halide perovskite nanocrystals revealed by magneto-optical spectroscopy. *Nano Lett.* **17**, 2895–2901 (2017).
19. Isarov, M., Tan, L. Z., Bodnarchuk, M. I., Kovalenko, M. V., Rappe, A.M. and Lifshitz, E. Rashba effect in a single colloidal $CsPbBr_3$ perovskite nanocrystal detected by magneto-optical measurements. *Nano Lett.* **17**, 5020–5026 (2017).
20. Canneson, D., Shornikova, E. V., Yakovlev, D. R., Rogge, T., Mitioglu, A. A., Ballottin, M. V., Christianen, P. C. M., Lhuillier, E., Bayer, M., Biadala, L. Negatively charged and dark excitons in $CsPbBr_3$ perovskite nanocrystals revealed by high magnetic fields. *Nano Lett.* **17**, 6177–6183 (2017).
21. Nestoklon, M. O., Goupalov, S. V., Dzhioev, R. I., Ken, O. S., Korenev, V. L., Kusrayev, Yu. G., Sapega, V. F., de Weerd, C., Gomez, L., Gregorkiewicz, T., Lin, J., Suenaga, K., Fujiwara, Y., Matyushkin, L. B., and Yassievich, I. N. Optical orientation and alignment of excitons in ensembles of inorganic perovskite nanocrystals. *Phys. Rev. B* **97**, 235304 (2018).
22. Crane, M. J., Jacoby, L. M., Cohen, T. A., Huang, Y., Luscombe, C. K. and Gamelin, D. R. Coherent spin precession and lifetime-limited spin dephasing in $CsPbBr_3$ perovskite nanocrystals. *Nano Lett.* **20**, 8626–8633 (2020).
23. Grigoryev, P. S., Belykh, V. V., Yakovlev, D. R., Lhuillier, E. and Bayer M. Coherent spin dynamics of electrons and holes in $CsPbBr_3$ colloidal nanocrystals. *Nano Lett.* **21**, 8481–8487 (2021).
24. Strohmair, S., Dey, A., Tong, Y., Polavarapu, L., Bohn, B. J. and Feldmann, J. Spin polarization dynamics of free charge carriers in $CsPbI_3$ nanocrystals. *Nano Lett.* **20**, 4724–4730 (2020).
25. Chen, D., Yuan, S., Chen, J., Zhong, J., and Xu, X. Robust $CsPbX_3$ (X = Cl, Br, and I) perovskite quantum dot embedded glasses. *J. Mater. Chem. C* **47**, 12864–12870 (2018).
26. Kolobkova, E. V., Kuznetsova, M. S. and Nikonorov, N. V. Perovskite $CsPbX_3$ (X=Cl, Br, I) nanocrystals in fluorophosphate glasses. *J. Non-Cryst. Solids* **563**, 120811 (2021).
27. Frost, J. M., Butler, K. T., Brivio, F., Hendon, C. H., van Schilfgaarde, M., and Walsh, A. Atomistic origins of high-performance in hybrid halide perovskite solar cells. *Nano Lett.* **14**, 2584–2590 (2014).
28. Zhang, Y.-Y., Chen, S., Xu, P., Xiang, H., Gong, X.-G., Walsh, A. and Wei, S.-H. Intrinsic instability of the hybrid halide perovskite semiconductor $CH_3NH_3PbI_3$. *Chinese Phys. Lett.* **3**, 036104 (2018).
29. Krieg, F., Sercel, P. C., Burian, M., Andrusiv, H., Bodnarchuk, M. I., Stöferle, T., Mahrt, R. F., Naumenko, D. Amenitsch, H., Raino, G. and Kovalenko, M. V. Monodisperse long-chain sulfobetaine-capped $CsPbBr_3$ nanocrystals and their superfluorescent assemblies. *ACS Central Science* **7**, 135–144 (2021).
30. Press, D., Ladd, T. D., Zhang, B. and Yamamoto, Y. Complete quantum control of a single quantum dot spin using ultrafast optical pulses. *Nature* **456**, 218–221 (2008).
31. Greilich, A., Economou, Sophia E., Spatzek, S., Yakovlev, D. R., Reuter, D., Wieck, A. D., Reinecke, T. L. and Bayer, M. Ultrafast optical rotations of electron spins in quantum dots. *Nature Phys.* **5**, 262–266 (2009).
32. Greilich, A., Yakovlev, D. R., Shabaev, A., Efros, Al. L., Yugova, I. A., Oulton, R., Stavarache, V., Reuter, D., Wieck, A. and Bayer, M. Mode locking of electron spin coherences in singly charged quantum dots. *Science* **313**, 341–345 (2006).
33. Greilich, A., Shabaev, A., Yakovlev, D. R., Efros, Al. L., Yugova, I. A., Reuter, D., Wieck, A. D. and Bayer, M. Nuclei-induced frequency focusing of electron spin coherence. *Science* **317**, 1896–1899 (2007).
34. Yakovlev, D. R. and Bayer, M. Coherent spin dynamics of carriers, Chapter 6 in *Spin Physics in Semiconductors* (ed. Dyakonov, M. I.) pp. 155–206 (Springer International Publishing AG, 2017).
35. Evers, E., Kopteva, N. E., Yugova, I. A., Yakovlev, D. R., Bayer, M. and Greilich, A. Suppression of nuclear spin fluctuations in an InGaAs quantum dot ensemble by GHz-pulsed optical excitation. *npj Quantum Information* **7**, 60 (2021).
36. Evers, E., Kopteva, N. E., Yugova, I. A., Yakovlev, D. R., Bayer, M. and Greilich, A. Shielding of external magnetic field by dynamic nuclear polarization in (In,Ga)As quantum dots. *Phys. Rev. B* **104**, 075302 (2021).
37. Yugova, I. A., Glazov, M. M., Yakovlev, D. R., Sokolova, A. A. and Bayer, M. Coherent spin dynamics of electrons and holes in semiconductor quantum wells and quantum dots under periodical optical excitation: Resonant spin amplification versus spin mode locking. *Phys. Rev. B* **85**, 125304 (2012).
38. Belykh, V. V., Yakovlev, D. R., Glazov, M. M., Grigoryev, P. S., Hussain, M., Rautert, J., Dirin, D. N., Kovalenko, M. V. and Bayer, M. Coherent spin dynamics of electrons and holes in $CsPbBr_3$ perovskite crystals. *Nat. Commun.* **10**, 673 (2019).
39. Kirstein, E., Yakovlev, D. R., Glazov, M. M., Evers, E., Zhukov, E. A., Belykh, V. V., Kopteva, N. E., Kudlacik, D., Nazarenko, O., Dirin, D. N., Kovalenko, M. V. and

Bayer, M. Lead-dominated hyperfine interaction impacting the carrier spin dynamics in halide perovskites. *Advanced Materials* **34**, 2105263 (2022).

40. Kirstein, E., Yakovlev, D. R., Glazov, M. M., Zhukov, E. A., Kudlacik, D., Kalitukha, I. V., Sapega, V. F., Dimitriev, G. S., Semina, M. A., Nestoklon, M. O., Ivchenko, E. L., Kopteva, N. E., Dirin, D. N., Nazarenko, O., Kovalenko, M. V., Baumann, A., Höcker, J., Dyakonov, V. and Bayer, M. The Landé factors of electrons and holes in lead halide perovskites: universal dependence on the band gap. http://arxiv.org/abs/2112.15384, 31 December 2021.
41. Odenthal, P., Talmadge, W., Gundlach, N., Wang, R., Zhang, C., Sun, D., Yu, Z.-G., Vardeny, V. Z. and Li, Y. S. Spin-polarized exciton quantum beating in hybrid organic–inorganic perovskites. *Nature Physics* **13**, 894 (2017).
42. Garcia-Arellano, G., Trippé-Allard, G., Legrand, L., Barisien, T., Garrot, D., Deleporte, E., Bernardot, F., Testelin, C. and Chamarro, M. Energy tuning of electronic spin coherent evolution in methylammonium lead iodide perovskites. *J. Phys. Chem. Lett.* **12**, 8272 (2021).
43. Smirnov, D. S., Zhukov, E. A., Yakovlev, D. R., Kirstein, E., Bayer, M. and Greilich, A. Spin polarization recovery and Hanle effect for charge carriers interacting with nuclear spins in semiconductors. *Phys. Rev. B* **102**, 235413 (2020).
44. Varwig, S., Schwan, A., Barmscheid, D., Müller, C., Greilich, A., Yugova, I. A., Yakovlev, D. R., Reuter, D., Wieck, A. D. and Bayer, M. Hole spin precession in a (In,Ga)As quantum dot ensemble: From resonant spin amplification to spin mode locking, *Phys. Rev. B* **86**, 075321 (2012).
45. Glazov, M. M. *Electron & Nuclear Spin Dynamics in Semiconductor Nanostructures* (Oxford University Press, Oxford, UK, 2018).
46. Kalevich, V. K. and Korenev, V. L. Optical polarization of nuclei and ODNMR in GaAs/AlGaAs quantum wells. *Appl. Magn. Reson.* **2**, 397 (1991).
47. Yugova, I. A., Glazov, M. M., Ivchenko, E. L. and Efros, Al. L. Pump-probe Faraday rotation and ellipticity in an ensemble of singly charged quantum dots. *Phys. Rev. B.* **80**, 104436 (2009).
48. Fras, F. and Eble, B. and Siarry, B. and Bernardot, F. and Miard, A. and Lemaître, A. and Testelin, C. and Chamarro, M. Hole spin mode locking and coherent dynamics in a largely inhomogeneous ensemble of *p*-doped InAs quantum dots. *Phys. Rev. B* **86**, 161303(R) (2012).
49. Dong, Y., Qiao, T., Kim, D., Parobek, D., Rossi, D. and Son, D. H. Precise control of quantum confinement in cesium lead halide perovskite quantum dots via thermodynamic equilibrium. *Nano Lett.* **6**, 3716–3722 (2018).
50. Heisterkamp, F., Kirstein, E., Greilich, A., Zhukov, E. A., Kazimierczuk, T., Yakovlev, D. R., Pawlis, A. and Bayer, M. Dynamics of nuclear spin polarization induced and detected by coherently precessing electron spins in fluorine-doped ZnSe. *Phys. Rev. B* **93**, 081409 (2016).

Supplementary Information: Mode locking of hole spin coherences in $CsPb(Cl,Br)_3$ perovskite nanocrystals

E. Kirstein, N. E. Kopteva, D. R. Yakovlev, E. A. Zhukov, E. V. Kolobkova, M. S. Kuznetsova, V. V. Belykh, I. A. Yugova, M. M. Glazov, M. Bayer, and A. Greilich

S1: HOLE g-FACTOR IN NANOCRYSTALS IN COMPARISON WITH UNIVERSAL DEPENDENCE ON BAND GAP FOR BULK PEROVSKITES

For convenient comparison of the g-factors in NCs with bulk perovskites, we use for the NCs the same approach for definition of the g-factor sign as in bulk, see e.g. Refs. [S1–S3]. In this definition the g-factors are positive both for electrons and holes when their ground state is the state with spin projection $S_z = -1/2$ onto the direction of the magnetic field. In this approach the exciton g-factor $g_X = g_e + g_h$. We used the same approach in our recent paper on electron and hole spin coherence in $CsPbBr_3$ NCs [S4], while in our earlier paper [S5] on polarized photoluminescence in strong magnetic fields from $CsPbBr_3$ NCs another approach, common for colloidal NCs [S6], was taken, which gives the opposite sign for the hole g-factor. Figure S1 shows the experimentally measured values of g-factors for electrons and holes in perovskite crystals versus the corresponding band gap energies (E_g). The hole g-factor value $g_h = +1.20$ in $CsPb(Cl,Br)_3$ NCs from the present study coincides well with the expected behavior.

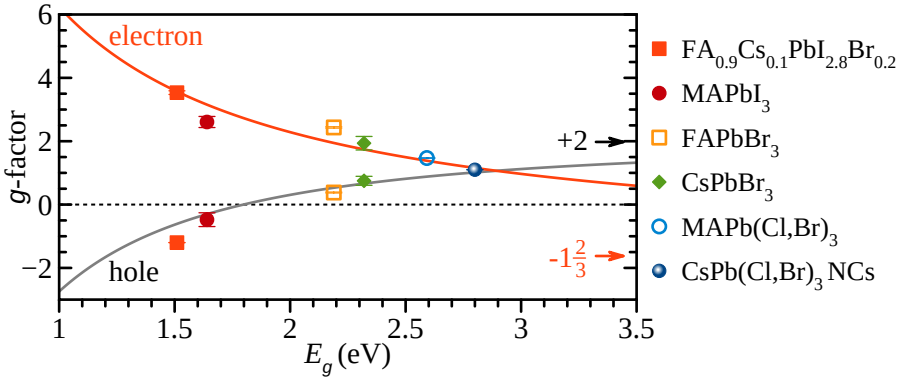

Supplementary Figure S1. **Electron and hole g-factors versus band gap energy in lead halide perovskite crystals.** Experimental data for various bulk perovskites measured at $T = 1.6$ and 5 K are taken from Ref. [S7] and shown by the symbols with error bars. Solid lines are model calculations, for details see Ref. [S7]. The limiting values of the electron ($-5/2$) and hole ($+2$) g-factors for $E_g \to \infty$ are given by the arrows. Blue circle shows the hole g-factor in the $CsPb(Cl_{0.5}Br_{0.5})_3$ NCs with $g_h = +1.20$, measured in the present study.

S2: DYNAMIC NUCLEAR POLARIZATION IN PEROVSKITES WITH $g_e > 0$ AND $g_h > 0$

Let us consider dynamic nuclear polarization by spin-oriented holes. It can not be realized in the Voigt geometry, as one need to have finite projection of the hole spin polarization on the direction of external magnetic field **B** (Fig. S2). The circularly polarized pump pulses orient the hole spin (i.e. generate the hole spin polarization) along the direction of the k-vector of light (i.e. along the optical axis), see the green arrows in Fig. S2. The hole spin polarization **S** is transferred by flip-flop processes to the nuclear spin system. The nuclear polarization **I** is collinear with the external magnetic field **B** and its orientation is controlled by orientation of **S**, i.e. can be controlled by the pump helicity. The oriented nuclear spins (**I**) create an effective magnetic field acting back on the hole spins – the Overhauser field ($\mathbf{B}_N$) [S8]. If the hole spin is in a tilted external magnetic field (**B**), the Overhauser field has a nonzero projection onto the direction of the external field and consequently increases or decreases the Larmor frequency of the hole spin precession. This depends on the pump circular polarization and therefore on the initial hole spin orientation, see Fig. S2.

Supplementary Table S1. Major abundant non-zero nuclear spin isotopes in $CsPb(Cl,Br)_3$. The table columns give: isotope name, natural abundance α, nuclear spin I, magnetic dipole moment of the isotope μ normalized to the nuclear magneton μ_N, gyromagnetic ratio γ. Note that $\mu = g_N \mu_N$ and $\gamma = g_N \mu_N / \hbar$, where g_N is nuclear g-factor.

isotope	α	I	μ/μ_N	γ [MHz/T]
^{133}Cs	100%	7/2	2.58	5.623
^{207}Pb	22.1%	1/2	0.58	8.882
^{35}Cl	75.8%	3/2	0.82	4.176
^{37}Cl	24.2%	3/2	0.68	3.476
^{79}Br	50.7%	3/2	2.10	10.704
^{81}Br	49.3%	3/2	2.27	11.538

Note that for $CsPb(Cl,Br)_3$ NCs, where electron and hole g-factors are positive ($g_e > 0$ and $g_h > 0$), the schemes shown in Fig. S2 are same for the electron and hole. Change of the g-factor sign invert the direction of the carrier spin polarization **S** and, respectively, the direction of the nuclear polarization **I**.

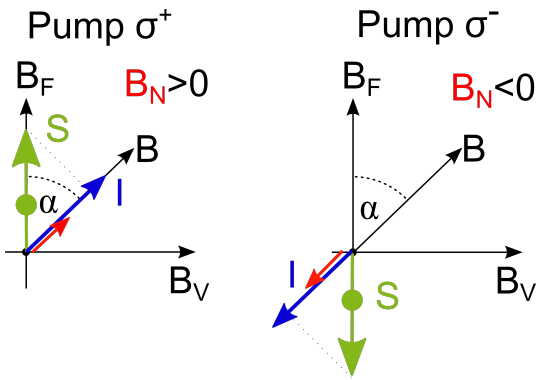

Supplementary Figure S2. **Dynamic nuclear polarization in perovskites with $g_e > 0$ and $g_h > 0$ in tilted magnetic field.** Scheme of interaction of charge carrier spins with nuclear spin system (identical for electrons and holes). Optically polarized carriers transfer their spin to the nuclei and induce nuclear spin polarization **I**. In turn, the nuclear polarization causes an Overhauser field, $\mathbf{B}_N$, acting back on the carriers. Orientation of the carrier spin polarization **S** (green arrow) is determined by the light helicity, σ^+ (σ^-) polarizations causes spin up (down), shown in the left and right panels, respectively. The nuclear polarization **I** (blue arrow) builds up in the direction of **S**, along the magnetic field **B** (black arrow). Here the magnetic field is inclined relative to the carrier spin polarization by an angle α. For a σ^+ polarized pump, the nuclear spin polarization manifests as Overhauser field $\mathbf{B}_N$ (red arrow), which is directed along **I** and along **B**. For a σ^- polarized pump $\mathbf{B}_N$ and **B** are antiparallel to each other.

Which nuclear spins are affected by the carrier spins, depends on various parameters [S3]. The most important ones for the abundant non-zero nuclear spin isotopes in $CsPb(Cl,Br)_3$ are given in Tab. S1.

S3: TEMPERATURE DEPENDENCE OF HOLE SPIN MODE LOCKING

As our previous studies show [S1], the efficiency of the dynamic nuclear polarization strongly depends on temperature and excitation power, which should also be seen via decreased efficiency of NIFF. In the case of the studied perovskite NCs, a temperature increase from $T = 1.6\,\mathrm{K}$ to $5.3\,\mathrm{K}$ results in a loss of the SML signal amplitude at negative delay times in the TRFE signal (Fig. S3). Taking into account the strong hole localization and constant pump power, we associate this effect with reduction of the NIFF effect and/or shortening of the hole spin coherence time T_2. This leads to a decrease of the hole SML amplitude for $T_2 \leq T_R$, as was observed in (In,Ga)As/GaAs quantum dots [S10, S11].

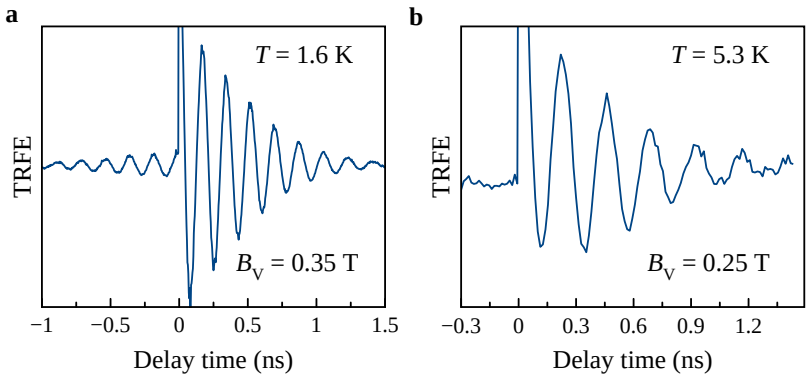

Supplementary Figure S3. **Temperature dependence of hole spin mode locking.** Time-resolved Faraday ellipticity signal measured at $E_{\rm pu} = 2.737\,$eV in the one-pump protocol. **a**, $B_{\rm V} = 0.35\,$T and $T = 1.6\,$K. **b**, $B_{\rm V} = 0.25\,$T and $T = 5.3\,$K. Pump helicity was modulated at a frequency $f_m = 10$ kHz.

S4: SPIN DEPHASING AND SPIN RELAXATION OF HOLES IN CsPb(Cl,Br)$_3$ NANOCRYSTALS

Figure S3 shows the TRFE signal revealing a single-frequency damped oscillation at $T = 5.3$ K and $B_{\rm V} = 0.25$ T. The magnetic field dependence of the Larmor precession frequency $\omega_{\rm L}$ is shown in Fig. S4**a**. The dependence of $\omega_{\rm L}(B_{\rm V})$ is linear without any offset at zero field, $\omega_{\rm L} = |g_h|\mu_B B_{\rm V}/\hbar$. It allows us to determine the hole g-factor value of $|g_h| = 1.20$ in the CsPb(Cl$_{0.5}$Br$_{0.5}$)$_3$ NCs. The right axis in Fig. S4**a** shows the value of the hole Zeeman splitting $E_Z = \hbar\omega_{\rm L}$. According to the theoretical dependence of the g-factor on the band gap, given in Supplementary Sec. S1, we assign a positive sign to the hole g-factor. The hole spin dephasing time T_2^* shortens with increase of $B_{\rm V}$ due to an increased precession phase mismatch caused by the g-factor spread Δg (Fig. S4b). This dependence can be described by the equation:

$$T_2^* = \frac{\hbar}{\sqrt{(\Delta g \mu_B B_{\rm V})^2 + (g_h \mu_B \Delta B)^2}}, \tag{S1}$$

from which the spread of g-factors $\Delta g = 0.03$ and the spin dephasing time $T_2^*(B_{\rm V} = 0) = \hbar/(g_h\mu_B\Delta B) = 0.5\,$ns due to the hole spin relaxation in zero external magnetic field by the nuclear spin fluctuation field $\Delta B = 20\,$mT are determined. Figure S4c presents the spin dephasing rate $1/T_2^*$ as function of applied magnetic field.

In zero magnetic field, the hole spin polarization relaxes due to interaction with random nuclear spin fluctuations. However, application of an external longitudinal magnetic field along the optical axis leads to a restoration of the spin

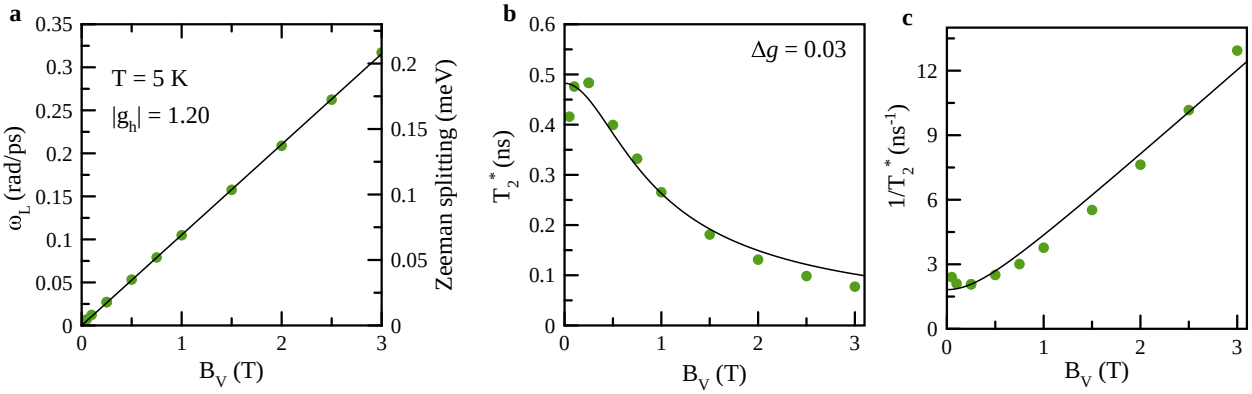

Supplementary Figure S4. **Magnetic field dependencies. a**, Magnetic field dependence of the Larmor precession frequency measured at $T = 5$ K for pump photon energy of 2.737 eV (green circles), $f_m = 10$ kHz. Linear fit (solid line) gives $|g_h| = 1.20$. **b**, Spin dephasing time T_2^* and **c**, spin dephasing rate $1/T_2^*$, as functions of the magnetic field measured at $T = 5$ K. Lines are fits with Eq. (S1), using the parameters $T_2^*(B_{\rm V} = 0) = 0.5\,$ns and $\Delta g = 0.03$.

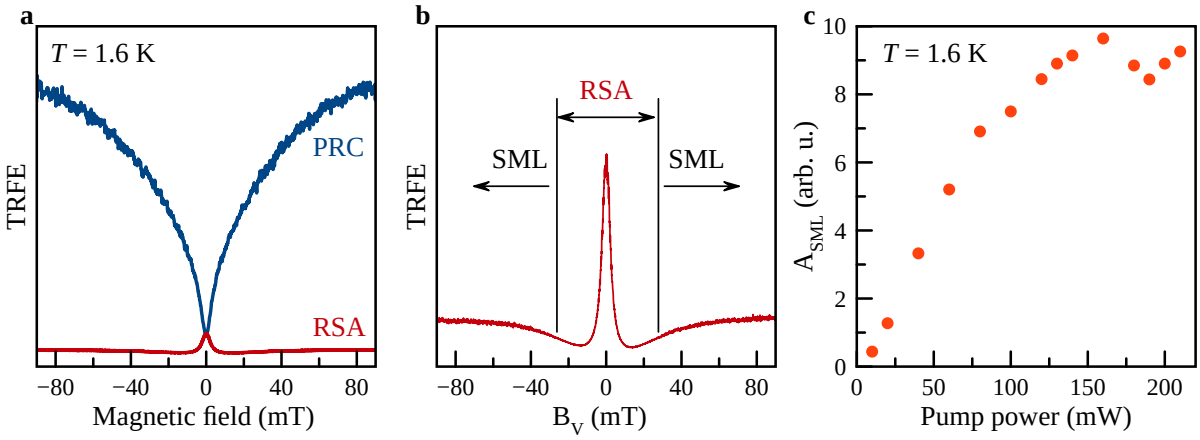

Supplementary Figure S5. **PRC and RSA dependencies.** **a**, PRC (blue) measured in B_{F}, and RSA (red) measured in B_{V} at the negative probe delay $t = -10$ ps for $T = 1.6$ K. Laser photon energy is 2.737 eV, pump power is 20 mW at the modulation frequency of $f_m = 10$ kHz. **b**, Zoom of the RSA signal from panel **a**. With increasing magnetic field the RSA regime is changing over to the SML regime. **c**, Spin mode locking amplitude A_{SML} at $t < 0$ as a function of the pump power measured in the one-pump protocol with $T_R = 13.2$ ns.

polarization as shown in Fig. S5a by the polarization recovery curve (PRC).

The spin polarization can be decreased by a transverse magnetic field. However, due to the pulsed excitation, when the spin of a resident carrier undergoes an integer number of revolutions about the external magnetic field between subsequent pump pulse arrivals, the magnitude of spin polarization measured close to zero delay increases again - this is the case of resonant spin amplification (RSA) [S22]. If the spin ensemble has a significant spread of g-factors, the RSA effect occurs only in a narrow range of magnetic fields around zero. Further increase of the magnetic field leads to an increasing number of possible PSC precessing modes, and the polarization magnitude becomes nonzero, reaching a constant value - the SML effect, as shown in Fig. S5a and its zoom in Fig. S5b. Such a transition of the hole spin system from RSA to SML was reported before for (In,Ga)As quantum dots with p-type doping [S12].

The SML effect strongly depends on the pump power, as shown in Fig. S5c. The SML amplitude increases and reaches saturation as the pump power increases. We did not observe in perovskite NCs Rabi oscillations, which have been reported for singly-charged (In,Ga)As quantum dots [S13]. Their absence is related to the pronounced inhomogeneity of the studied system.

To complete the characterization of the spin dynamics we have measured the longitudinal spin relaxation time T_1, using the spin inertia technique, see Fig. S6 [S14, S15]. Here, we alternate the pump helicity between σ^+ and σ^- and measure the spin polarization response with respect to the frequency of modulation, f_{m}. By increasing the frequency one can enter a regime where the modulation period is shorter than the spin relaxation time T_1. Thus the signal amplitude drops [S14]. The decay of the ellipticity upon increasing f_{m} can be described by the dependence $S(f_{\mathrm{m}}) = S_0/\sqrt{1+(2\pi f_{\mathrm{m}} T_s)^2}$, where T_s is the effective spin lifetime at the corresponding pump power. The extrapolation of T_s to zero power allows for extracting the intrinsic spin relaxation T_1 of the carriers. Figures. S6(b) and S6(c) depict the extracted times for two components present in the spin-inertia dependence. We relate them to two subsets of carriers in the NC ensemble and focus on the regime $f_{\mathrm{m}} \geq 10$ kHz for which only the shorter living component with $T_1 = 7.6\,\mu$s contributes significantly.

S5: THEORY OF SPIN MODE LOCKING. INTRODUCTION

The theory of spin mode locking was previously developed for singly charged epitaxial quantum dots [S22] and successfully applied to model experimental data in (In,Ga)As QDs [S12, S13]. However, discovering spin-locked modes in perovskite nanocrystals has provided new theoretical challenges. First, the generation of spin coherence in perovskite structures with an inverted band structure occurs on the basis of modified selection rules. Circularly polarized light generates excitons with an electron ($S = 1/2$) and a hole ($S = 1/2$), instead of an exciton with an electron ($S = 1/2$) and a heavy hole ($S = 3/2$). Second, an ensemble of perovskite colloidal nanocrystals has a random orientation of the c-axis, which leads to less efficient generation of hole spin polarization along the optical axis. The

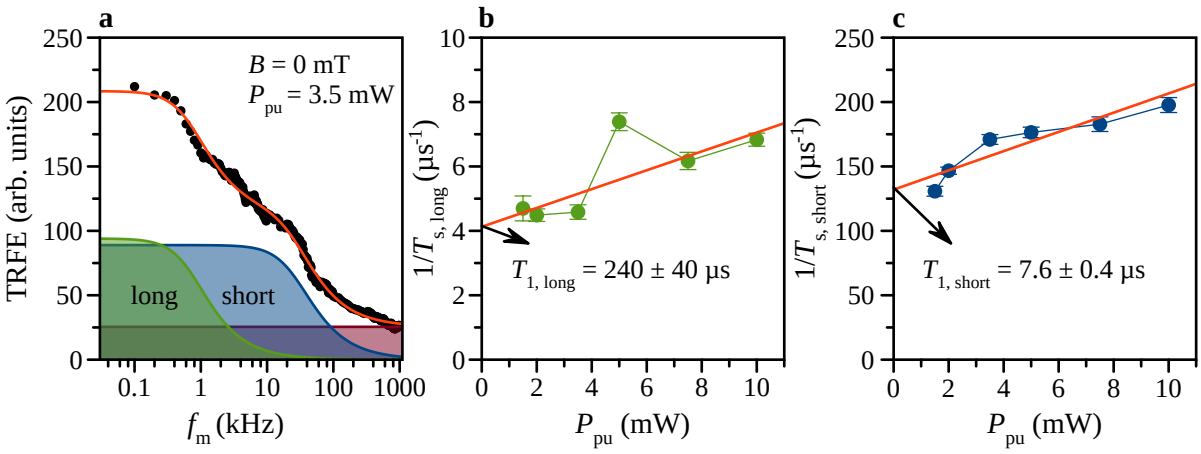

Supplementary Figure S6. **Spin inertia. a**, Faraday ellipticity amplitude as a function of the pump modulation frequency f_{m} for a pump power of $P_{\mathrm{pu}} = 3.5\,\mathrm{mW}$ measured at a magnetic field of $B = 0\,\mathrm{mT}$ with a pump-probe delay of $-10\,\mathrm{ps}$ (black circles). The red line is the two-component fit. The contributions of each component are shown by the green-shaded and blue-shaded areas. The violet-shaded area gives the frequency independent offset, that can be related to the scattered light. **b–c**, The power dependence of the two corresponding inverse effective spin lifetimes $1/T_s$. A linear extrapolation to zero power (red lines) yields $T_{1,\mathrm{long}} = (240 \pm 40)\,\mu\mathrm{s}$ (**b**) and $T_{1,\mathrm{short}} = (7.6 \pm 0.4)\,\mu\mathrm{s}$ (**c**). $T = 1.6\,\mathrm{K}$. All error bars are given by the standard deviations from the fits.

anisotropy c-axis is typical for the low temperatures when the perovskite materials expose structural transition from cubic to tetragonal or orthorhombic phase. Third, due to the variety of perovskite materials, different nanocrystal samples may have different crystal symmetries, which is also considered in the developed model, even though the calculations are performed here only for cubic symmetry. For a complete theoretical description, the anisotropy of g-factors for a single NC has to be considered, as well as the possibility of generating spin coherence through positively and negatively charged trions. In order to account for all these factors a considerable modification of the previously developed models of SML and NIFF need to be done.

The theoretical part is structured as follows:

1) Section S5 introduces the choice of the used coordinate systems.

2) In section S6 the generation of spin polarization of resident carriers (electron and hole) through intermediate trion state in a single NC is considered.

3) Section S7 considers the universal electron and hole spin polarization behavior in an external magnetic field for a single NC with an anisotropic g-factor.

4) Section S8 considers the inhomogeneity of the NC ensemble due to the g-factors dispersion and random orientation

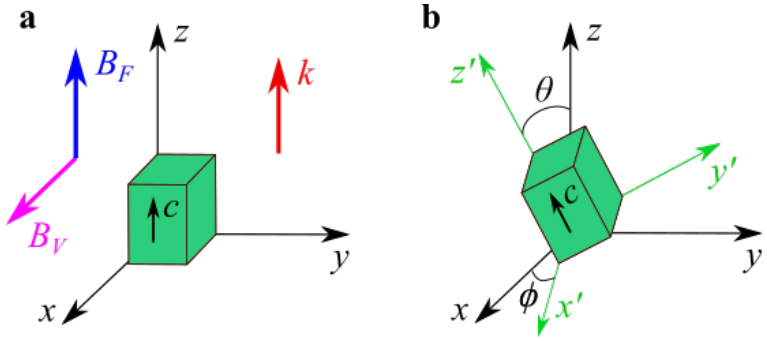

Supplementary Figure S7. **Laboratory and NC coordinate systems used for the calculations. a**, Laboratory coordinate system (x, y, z) where $\mathbf{k} \parallel z$, $\mathbf{B}_{\mathrm{F}} \parallel z$ and $\mathbf{B}_{\mathrm{V}} \parallel x$ for the Faraday and Voigt geometries, respectively. The green parallelepiped symbolizes a single nanocrystal with the c-axis oriented parallel to the k-vector ($c \parallel \mathbf{k}$). **b**, Illustration of the NC coordinate frame (x', y', z') tilted with respect to (x, y, z). Orientation angles $\sphericalangle(z, z') := \theta \in [0; \pi]$ and $\sphericalangle(x, x') := \phi \in [0; 2\pi]$ are defined as shown in the scheme.

of the NC axes.

5) The modeling of the experimental results is given in Sections S9 and S10.

Let us start the presentation of the theoretical model by introducing the coordinate systems. The laboratory coordinate system is taken as (x, y, z) where $\mathbf{k} \parallel z$, $\mathbf{B}_\mathrm{F} \parallel z$ and $\mathbf{B}_\mathrm{V} \parallel x$ for the Faraday and Voigt geometries, shown in Fig. S7a. The single nanocrystal with $c \parallel z$ is presented by the green parallelepiped. For this NC orientation, the Voigt geometry is $\mathbf{B}_\mathrm{V} \parallel x$ and $\mathbf{k} \parallel z$. The coordinate system (x', y', z') is associated with the NC axes and $c \parallel z'$ as shown in Fig. S7b. (x', y', z') is tilted in respect to (x, y, z) by the angles $\theta \in [0; \pi]$ and $\phi \in [0; 2\pi]$, for a NC with an arbitrary c-axis orientation. The final expressions for the spin polarization components are integrated over all possible projections of the external magnetic field and the light propagation direction on the NC axes, to simulate the random orientation of the NC axes relative to the laboratory coordinate system. One can project (x, y, z) on (x', y', z'):

$$x' = (x\cos\theta - z\sin\theta)\cos\phi + y\sin\phi, \tag{S2}$$

$$y' = -(x\cos\theta - z\sin\theta)\sin\phi + y\cos\phi, \tag{S3}$$

$$z' = z\cos\theta + x\sin\theta. \tag{S4}$$

We assume that the laser light propagates along z ($\mathbf{k} \parallel z$), so that its electric field component $E_z = 0$. Therefore, the electric field components in the NC coordinate system (x', y', z') are:

$$E_{x'} = E_x\cos\theta\cos\phi + E_y\sin\phi, \tag{S5}$$

$$E_{y'} = -E_x\cos\theta\sin\phi + E_y\cos\phi, \tag{S6}$$

$$E_{z'} = E_x\sin\theta. \tag{S7}$$

For the σ^+ circularly polarized light $E_x = iE_y$.

S6: OPTICAL GENERATION OF SPIN COHERENCE

This section considers the generation of spin polarization of resident carriers (electrons and holes) in a single NC via intermediate trion states using short optical pulses. Atomistic modeling [S17] shows that the s-orbitals of the metal (Pb) form the valence band with an admixture of the p-orbitals of the halogen (Br,Cl). The p-orbitals of the metal form the conduction band with an admixture of the halogen s-orbitals [S1]. Taking into account the spin-orbit interaction, the electron $\pm 1/2$ spin states in the conduction band and the hole $\pm 1/2$ spin states in the valence band determine the fundamental optical transitions [S1], see also Fig. S8.

The matrix elements of the momentum operator $\hat{p} = (p_\perp, p_\perp, p_\parallel)$ taken between the conduction band Bloch functions $|c.b., x\rangle$, $|c.b., y\rangle$ or $|c.b., z\rangle$ and the valence band $|v.b.\rangle$ Bloch functions at the R-point of the Brillouin zone are given by:

$$p_\perp = \langle c.b., x|\hat{p}_x|v.b.\rangle = \langle c.b., y|\hat{p}_y|v.b.\rangle, \quad p_\parallel = \langle c.b., z|\hat{p}_z|v.b.\rangle. \tag{S8}$$

A representation of the wave functions is given in Ref. [S1].

Pump excitation with circular polarization leads to creation of an exciton. However, as the excitons have short lifetimes (≈ 160 ps), the pump-probe signal at a nanosecond time scale is provided by resident carrier spins localized in the NCs. We assume that the NCs, being initially uncharged, become charged through the optical excitation, where one of the charges becomes trapped in the NC. This photocharging in long living and, when the next optical pulse generates an additional exciton, this leads to formation of a trion complex with the resident carrier. Figures S9b,c show level schemes of the photogeneration of negative and positive trions in a nanocrystal by σ^+ polarized excitation. If uncharged, σ^+ polarized light excites in the NC the conduction band state with wave function $c[+1/2]$ and the valence band state with wave function $v[+1/2]$, marked by $|\uparrow\rangle$ and $|\Uparrow\rangle$, respectively. If the nanocrystal contains a resident electron with wave function $c[-1/2]$, marked by $|\downarrow\rangle$, the light creates a negatively charged trion (T^-). In the case of a resident hole with a wave function $v[-1/2]$, marked by $|\Downarrow\rangle$, a positively charged trion (T^+) is generated.

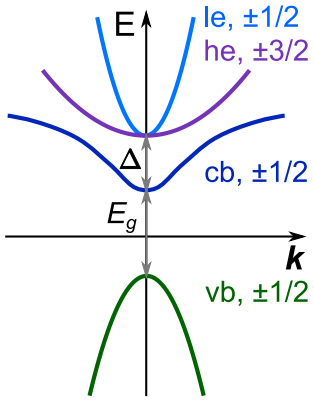

Supplementary Figure S8. **Schematics of perovskite band structure.** The spin ±1/2 valence band (vb) and the spin ±1/2 conduction band (cb) are separated by the optical band gap (E_g). Above the cb the heavy-electron (he) and light-electron (le) bands with spin ±3/2 and ±1/2, respectively, are located, set apart by the spin-orbit energy (Δ).

After the trion recombination, the spin of the resident carrier retains its polarization with a corresponding optical response in the pump-probe signal.

The matrix elements of the optical transitions created by the circularly polarized light from the electron states to the negative trion states are taken from the Ref. [S18], and for the negative trion (T^-) can be written as:

$$M_{T^-}(c[-1/2];v[+1/2]) \propto -\frac{\cos\xi}{\sqrt{2}}(E_{x'} - iE_{y'})p_\perp \propto d_1E_1, \tag{S9}$$

$$M_{T^-}(c[+1/2];v[-1/2]) \propto -\frac{\cos\xi}{\sqrt{2}}(E_{x'} + iE_{y'})p_\perp \propto d_2E_2, \tag{S10}$$

$$M_{T^-}(c[-1/2];v[-1/2]) \propto -\sin\xi E_{z'}p_\parallel \propto d_3E_3, \tag{S11}$$

$$M_{T^-}(c[+1/2];v[+1/2]) \propto \sin\xi E_{z'}p_\parallel \propto -d_3E_3. \tag{S12}$$

One should note that for the σ^+ circularly polarized light $E_x = iE_y$ in the laboratory coordinate system then $E_{x'} \pm iE_{y'} = E_x\exp(\mp i\phi)(\cos\theta \mp 1)$ in the NC coordinate system.

The matrix elements for σ^+ polarized light are:

$$d_1E_1 \propto -\frac{\cos\xi p_\perp}{\sqrt{2}}E_x\exp(i\phi)(\cos\theta + 1), \tag{S13}$$

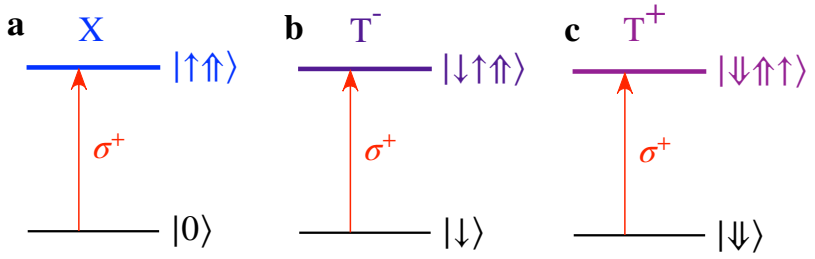

Supplementary Figure S9. Optical transitions for the generation by a σ^+ polarized photon of: (**a**) an exciton , (**b**) T^- , and (**c**) T^+. $|\uparrow\rangle$ and $|\downarrow\rangle$ indicate the electron states with the wave functions $c[+1/2]$ and $c[-1/2]$, respectively. $|\Uparrow\rangle$ and $|\Downarrow\rangle$ indicate the hole states with the wave functions $v[+1/2]$ and $v[-1/2]$, respectively. The trions are photogenerated in their ground state, which is a spin singlet of the electrons or holes.

$$d_2E_2 \propto -\frac{\cos\xi p_\perp}{\sqrt{2}}E_x\exp(-i\phi)(\cos\theta-1), \tag{S14}$$

$$d_3E_3 \propto -\sin\xi p_\parallel E_x\sin\theta. \tag{S15}$$

In the cubic approximation $\sin\xi = 1/\sqrt{3}$, $\cos\xi = \sqrt{2/3}$ and $p_\perp = p_\parallel = p$. The matrix elements of the optical transitions to a positive trion (T^+) are:

$$M_{T^+}(v[-1/2];c[+1/2]) = M_{T^-}(c[-1/2];v[+1/2]) \propto d_1E_1, \tag{S16}$$

$$M_{T^+}(v[+1/2];c[-1/2]) = M_{T^-}(c[+1/2];v[-1/2]) \propto d_2E_2, \tag{S17}$$

$$M_{T^+}(v[+1/2];c[+1/2]) = M_{T^-}(c[-1/2];v[-1/2]) \propto d_3E_3, \tag{S18}$$

$$M_{T^+}(v[-1/2];c[-1/2]) = M_{T^-}(c[+1/2];v[+1/2]) \propto -d_3E_3. \tag{S19}$$

The Hamiltonian of the interaction of the nanocrystal with light in the basis ($c[1/2]$; $c[-1/2]$; $v[1/2]$; $v[-1/2]$) for T^- creation is represented by:

$$\hat{H} = \frac{\hbar}{2}\begin{pmatrix} 0 & 0 & -f_3^*e^{i\omega t} & f_2^*e^{i\omega t} \\ 0 & 0 & f_1^*e^{i\omega t} & f_3^*e^{i\omega t} \\ -f_3e^{-i\omega t} & f_1e^{-i\omega t} & 0 & 0 \\ f_2e^{-i\omega t} & f_3e^{-i\omega t} & 0 & 0 \end{pmatrix}. \tag{S20}$$

Here $\hbar$ is the reduced Planck constant, ω is the optical frequency of the light, t is the time, $f_i(t) = -\frac{2e^{i\omega t}}{\hbar}\int d_i(\mathbf{r})E_i(\mathbf{r},t)d^3r$ is the time-dependent matrix element for description of the light interaction with a nanocrystal with index $i = (1,2,3)$. For T^+ in the basis ($v[1/2]$; $v[-1/2]$; $c[1/2]$; $c[-1/2]$) one needs to change the sign of f_3 in the Hamiltonian (S20). One can introduce the analytical expressions for the matrix element describing the interaction with a σ^+ circularly polarized optical pulse with duration τ_p and pulse area Θ:

$$f_1\tau_p \propto -\frac{\Theta}{2}e^{i\phi}(\cos\theta+1), \tag{S21}$$

$$f_2\tau_p \propto \frac{\Theta}{2}e^{-i\phi}(\cos\theta-1), \tag{S22}$$

$$f_3\tau_p \propto \frac{\Theta}{2}\alpha\sin\theta. \tag{S23}$$

Here $\alpha = p_\parallel\sqrt{2}\tan\xi/p_\perp$, in cubic approximation $\alpha = 1$. Therefore, a short pulse with rectangular shape changes the wave functions ψ_1^b and ψ_2^b of the electron in the conduction band $c[1/2]$ and $c[-1/2]$, respectively, to the wave functions after pulse action ψ_1^a and ψ_2^a. Here index 'b' stands for 'before' and 'a' for 'after' pulse action:

$$\psi_1^a = \frac{e^{i\omega'\tau_p/2}}{2}\left[\psi_1^b\left(K_p\left[1+\frac{\Delta}{W}\right]+K_m\left[1-\frac{\Delta}{W}\right]\right)+\psi_2^b\frac{2\Pi}{W}(K_p-K_m)\right], \tag{S24}$$

$$\psi_2^a = \frac{e^{i\omega'\tau_p/2}}{2}\left[\psi_2^b\left(K_m\left[1+\frac{\Delta}{W}\right]+K_p\left[1-\frac{\Delta}{W}\right]\right)+\psi_1^b\frac{2\Pi^*}{W}(K_p-K_m)\right]. \tag{S25}$$

$\omega' = \omega_p - \omega_0$ is the optical detuning between the pulse central frequency ω_p and the trion resonant frequency ω_0. Δ and Π are coefficients composed from f_i:

$$\Delta = \frac{1}{4}(|f_2|^2-|f_1|^2) = -\frac{|\Theta|^2}{4}\cos\theta, \tag{S26}$$

$$\Pi = \frac{1}{4}(-f_1^* f_3 + f_2 f_3^*) = \mp\frac{|\Theta|^2}{8}\alpha \sin\theta \exp(-i\phi). \tag{S27}$$

The upper sign in Eq. (S27) corresponds to T^-, and the lower one corresponds to T^+.

$$W = \sqrt{\Delta^2 + 4|\Pi|^2}, \tag{S28}$$

$$K_{p,m} = \cos\left(\frac{\Omega_{p,m}\tau_p}{2}\right) - \frac{i\omega'}{\Omega_{p,m}}\sin\left(\frac{\Omega_{p,m}\tau_p}{2}\right), \tag{S29}$$

$$\Omega_{p,m} = \sqrt{(\omega')^2 + \frac{1}{2}(|f_1|^2 + |f_2|^2 + 2|f_3|^2) \pm 2W}. \tag{S30}$$

Ω corresponds to the Rabi oscillation frequency. In the cubic approximation $\Omega\tau_p = \sqrt{(\omega'\tau_p)^2 + \Theta^2}$.

A short circularly polarized pump pulse changes the resident hole spin polarization components in a single NC according to the equations:

$$\mathbf{S}^a = \mathcal{A}\cdot\mathbf{S}^b + \mathbf{S}_0 \tag{S31}$$

$$\mathcal{A} = \begin{pmatrix} \mathcal{A}_{11} & \mathcal{A}_{12} & \mathcal{A}_{13} \\ \mathcal{A}_{21} & \mathcal{A}_{22} & \mathcal{A}_{23} \\ \mathcal{A}_{31} & \mathcal{A}_{32} & \mathcal{A}_{33} \end{pmatrix}, \tag{S32}$$

$$\mathbf{S}_0 = \begin{pmatrix} S_{x',0} \\ S_{y',0} \\ S_{z',0} \end{pmatrix}, \qquad \mathbf{S}^a = \begin{pmatrix} S^a_{x'} \\ S^a_{y'} \\ S^a_{z'} \end{pmatrix}, \qquad \mathbf{S}^b = \begin{pmatrix} S^b_{x'} \\ S^b_{y'} \\ S^b_{z'} \end{pmatrix}. \tag{S33}$$

$\mathbf{S}^a$ is the spin polarization after the pulse arrival, $\mathbf{S}^b$ is the spin polarization before the pulse arrival.

$$\mathcal{A}_{11} = [|K_p + K_m|^2 - \frac{(\Delta^2 - 4\mathrm{Re}(\Pi^2))}{W^2}|K_p - K_m|^2]/4, \tag{S34}$$

$$\mathcal{A}_{12} = \frac{\Delta}{W}\mathrm{Im}(K_p K_m^*) - \frac{\mathrm{Im}(\Pi^2)}{W^2}|K_p - K_m|^2, \tag{S35}$$

$$\mathcal{A}_{13} = \frac{2\mathrm{Im}(\Pi)}{W}\mathrm{Im}(K_p K_m^*) + \frac{\Delta}{W^2}\mathrm{Re}(\Pi)|K_p - K_m|^2, \tag{S36}$$

$$\mathcal{A}_{21} = -\frac{\Delta}{W}\mathrm{Im}(K_p K_m^*) - \frac{\mathrm{Im}(\Pi^2)}{W^2}|K_p - K_m|^2, \tag{S37}$$

$$\mathcal{A}_{22} = [|K_p + K_m|^2 - \frac{(\Delta^2 + 4\mathrm{Re}(\Pi^2))}{W^2}|K_p - K_m|^2]/4, \tag{S38}$$

$$\mathcal{A}_{23} = \frac{2Re(\Pi)}{W}\mathrm{Im}(K_p K_m^*) - \frac{\Delta}{W^2}\mathrm{Im}(\Pi)|K_p - K_m|^2, \tag{S39}$$

$$\mathcal{A}_{31} = \frac{-2\mathrm{Im}(\Pi)}{W}\mathrm{Im}(K_p K_m^*) + \frac{\Delta}{W^2}\mathrm{Re}(\Pi)|K_p - K_m|^2, \tag{S40}$$

$$\mathcal{A}_{32} = -\frac{2\mathrm{Re}(\Pi)}{W}Im(K_p K_m^*) - \frac{\Delta}{W^2}\mathrm{Im}(\Pi)|K_p - K_m|^2, \tag{S41}$$

$$\mathcal{A}_{33} = [|K_p + K_m|^2 + \frac{(\Delta^2 - 4|\Pi|^2)}{W^2}|K_p - K_m|^2]/4, \tag{S42}$$

$$S_{x',0} = \frac{\mathrm{Re}(\Pi)}{2W}(|K_p|^2 - |K_m|^2), \tag{S43}$$

$$S_{y',0} = -\frac{\mathrm{Im}(\Pi)}{2W}(|K_p|^2 - |K_m|^2), \tag{S44}$$

$$S_{z',0} = \frac{\Delta}{4W}(|K_p|^2 - |K_m|^2). \tag{S45}$$

Here $K_0 = Ke^{i\omega'} - K^*e^{-i\omega'}$, $N = -iK_0$, $|\Gamma|^2 = (K - e^{-i\omega'})(K^* - e^{i\omega'})$ and $|\Sigma|^2 = (K + e^{-i\omega'})(K^* + e^{i\omega'})$.

Eqs. (S31-S45) describe the generation of the electron and hole spin polarization by a short optical pulse in a single NC with random c-axis orientation.

S7: SPIN DYNAMICS IN EXTERNAL MAGNETIC FIELD

Here we describe the dynamics of the spin polarization in an external magnetic field. In a single NC, the hole or electron spin oriented by a circularly polarized pump pulse precesses about the external magnetic field, which can be described using a semiclassical approach [S19]:

$$\frac{d\mathbf{S}}{dt} = [\boldsymbol{\omega} \times \mathbf{S}]\,. \tag{S46}$$

Here $\boldsymbol{\omega} = (\omega_{x'}, \omega_{y'}, \omega_{z'})$ is the Larmor precession frequency. $\omega_i = \mu_B g_i B_i/\hbar$, here $i = (x', y', z')$ and $\boldsymbol{g} = (g_{x'}, g_{y'}, g_{z'})$ is the anisotropic g-factor. Let us define that $g_{x'} = g_{y'} = g_\perp$ and $g_{z'} = g_\parallel$. The magnetic field components on the axis of the nanocrystal for an orientation $\mathbf{B} \parallel x$ in the laboratory coordinate system are given by:

$$B_{x'} = B_x \cos\theta\cos\phi, \tag{S47}$$

$$B_{y'} = -B_x \cos\theta\sin\phi, \tag{S48}$$

$$B_{z'} = B_x \sin\theta. \tag{S49}$$

Eq. (S46) is written in a form that includes spin relaxation for an anisotropic g-factor in a single NC:

$$\mathbf{S}(t) = \mathcal{B}(t) \cdot \mathbf{S}^a, \tag{S50}$$

$$\mathcal{B}(t) = \begin{pmatrix} \mathcal{B}_{11} & \mathcal{B}_{12} & \mathcal{B}_{13} \\ \mathcal{B}_{21} & \mathcal{B}_{22} & \mathcal{B}_{23} \\ \mathcal{B}_{31} & \mathcal{B}_{32} & \mathcal{B}_{33} \end{pmatrix} \cdot \exp(-t/\tau_s), \tag{S51}$$

$$\mathcal{B}_{11} = \cos(\omega_\mathrm{L} t) + \frac{g_\perp^2}{\tilde{g}^2}\cos^2\theta\cos^2\phi[1 - \cos(\omega_\mathrm{L} t)], \tag{S52}$$

$$\mathcal{B}_{12} = -\left[\frac{g_\perp^2}{2\tilde{g}^2}\cos^2\theta\sin 2\phi\,[1 - \cos(\omega_\mathrm{L} t)] + \frac{g_\parallel}{\tilde{g}}\sin\theta\sin(\omega_\mathrm{L} t)\right], \tag{S53}$$

$$\mathcal{B}_{13} = \frac{g_\parallel g_\perp}{2\tilde{g}^2}\cos\phi\sin 2\theta\,[1 - \cos(\omega_\mathrm{L} t)] - \frac{g_\perp}{\tilde{g}}\sin\phi\cos\theta\sin(\omega_\mathrm{L} t), \tag{S54}$$

$$\mathcal{B}_{21} = \frac{g_\parallel}{\tilde{g}}\sin\theta\sin(\omega_\mathrm{L} t) - \frac{g_\perp^2}{2\tilde{g}^2}\cos^2\theta\sin 2\phi\,[1 - \cos(\omega_\mathrm{L} t)]\,, \tag{S55}$$

$$\mathcal{B}_{22} = \cos(\omega_{\rm L} t) + \frac{g_\perp^2}{\tilde{g}^2}\cos^2\theta\sin^2\phi\left[1-\cos(\omega_{\rm L} t)\right], \tag{S56}$$

$$\mathcal{B}_{23} = -\frac{g_\parallel g_\perp}{2\tilde{g}^2}\sin\phi\sin 2\theta\left[1-\cos(\omega_{\rm L} t)\right] - \frac{g_\perp}{\tilde{g}}\cos\theta\cos\phi\sin(\omega_{\rm L} t), \tag{S57}$$

$$\mathcal{B}_{31} = \frac{g_\parallel g_\perp}{2\tilde{g}^2}\cos\phi\sin 2\theta\left[1-\cos(\omega_{\rm L} t)\right] + \frac{g_\perp}{\tilde{g}}\cos\theta\sin\phi\sin(\omega_{\rm L} t), \tag{S58}$$

$$\mathcal{B}_{32} = \frac{g_\parallel g_\perp}{2\tilde{g}^2}\sin\phi\sin 2\theta\left[1-\cos(\omega_{\rm L} t)\right] + \frac{g_\perp}{\tilde{g}}\cos\theta\cos\phi\sin(\omega_{\rm L} t). \tag{S59}$$

$$\mathcal{B}_{33} = 1 - \frac{g_\perp^2}{\tilde{g}^2}\cos^2\theta\left[1-\cos(\omega_{\rm L} t)\right]. \tag{S60}$$

$\mathbf{S}(t)$ contains the time-dependent components of the electron or hole spin polarization. $\omega_{\rm L} = \mu_{\rm B}\tilde{g}B/\hbar$ is the Larmor precession frequency in the external magnetic field. $\tilde{g} = \sqrt{g_\perp^2\cos^2\theta + g_\parallel^2\sin^2\theta}$ is the effective g-factor. τ_s is the spin relaxation time. Here, the isotropic spin relaxation time is $\tau_s = T_2$. Also, we assume that the trion spin relaxation is faster than the spin relaxation of the resident carrier and since g-factors of the resident carrier and the unpaired carrier in the trion differ significantly, we can neglect the polarization "returning from the trion". As a result, the resident carrier gets polarized right after the trion is formed.

In the experiment, the pump pulse creates a spin polarization, which subsequently precess in the external magnetic field. If the carrier spins do not loose the polarization until the arrival of the next pulse, i.e. for $T_2 > T_{\rm R}$, then spin polarization is accumulated. It is possible to model the experiment by considering an infinite number of pulses with subsequent dynamics in the magnetic field [S20]:

$$\mathbf{S}^a = (\mathbf{I} - \mathcal{A}\mathcal{B})^{-1}\mathbf{S}_0, \tag{S61}$$

with $\mathbf{I}$ being the unity matrix.

S8: DISTRIBUTION OF ELECTRON (HOLE) LARMOR PRECESSION FREQUENCY IN ENSEMBLE OF NCS

The dispersion of g-factors (Δg) and nuclear spin fluctuations ($\Delta\omega_{\rm N} = g\mu_{\rm B}\Delta B/\hbar$) broadens the spectrum of Larmor frequencies in an ensemble of nanocrystals [S20]. The resulting spectral distribution can be described by a Gaussian function:

$$\rho(\omega_{\rm L}) = \exp\left[-\frac{(\omega_{\rm L}-\omega_{\rm L,0})^2}{2(\Delta\omega)^2}\right]. \tag{S62}$$

Here, $\omega_{\rm L,0}$ is the central Larmor frequency of the distribution and $\Delta\omega = \sqrt{(\Delta g\mu_{\rm B}B_{\rm V}/\hbar)^2 + (\Delta\omega_{\rm N})^2}$ is the frequency dispersion. In a strong external magnetic fields exceeding the exchange field of the nuclear spin fluctuations ($B_{\rm V} \gg \Delta B$) $\Delta\omega \approx \Delta g\mu_{\rm B}B_{\rm V}/\hbar$. Obviously, for electrons and holes $\Delta\omega$ and ΔB are different, as they have different g-factors and Δg, as well as different hyperfine constants describing their interaction with the nuclei [S1].

S9: MODELING OF SML IN PEROVSKITE NCS

The simulation of the spin dynamics is carried out in five steps:
1) For a single NC the spin polarization components are calculated after the action of a pump pulse.
2) The precession of the spin polarization in an external magnetic field is calculated for a single NC.
3) The polarization components after action of an infinitely long pulse sequence are calculated.
4) Steps 1 – 3 are repeated for all possible precession frequencies in the nanocrystal ensemble with certain g-factor dispersion.

Without loss of generality we consider resident holes in the NCs, that are created by photocharging. The pump-probe Faraday ellipticity signal is generated through a trion intermediate state for the resident hole spin polarization (details of spin coherence generation are given in Supplementary Note S6). The spin polarization components tilted relative to the direction of the external magnetic field precess in time and decay with the spin coherence time T_2. If $T_2 \geq T_R$, then the spin polarization accumulates being excited by an infinite sequence of optical pulses, as in the experiment (for details see Supplementary Note S7).

The SML is an ensemble effect being formed by adding a large number of oscillating signals with frequencies commensurate with the repetition rate of the laser pulses and $T_2 \geq T_\mathrm{R}$. Therefore, the model takes into account the spread of the g-factors (Supplementary Note S8). Numerical modeling has been performed according to Eqs. (S26-S62). The simulated spin polarization (S_a) distribution after an infinite number of optical pulses at $B_\mathrm{V} = 0.35$ T is shown in Fig. S10b. The width of the distribution is defined by $2\Delta g$ with $\Delta g = 0.06$, the multiple peaks correspond to precession modes, and the width of each peak is determined by $1/T_2$. For simplicity we assume that the spin coherence time is isotropic and the same for all precession modes. The SML signal corresponding to the distribution is shown by red line in Fig. S10a compared to the experimental dynamics (black dots). The signal decay for negative and positive time delays is defined by Δg. The ratio S_b/S_a of the amplitudes before pulse arrival S_b and after pulse arrival S_a is determined by T_2, the optical pulse area Θ and also the NIFF effect which will be considered below in Supplementary Note S10. The numerical calculations show that integration over the angles ϕ and θ changes $\mathbf{S}_a$ and $\mathbf{S}_b$ in the same way. Therefore, the SML amplitude in case of cubic symmetry and the relative value S_b/S_a are independent of the random orientation of the crystals. The value S_b/S_a is, however, sensitive to the Rabi frequency $\Omega\tau_p = \sqrt{(\omega'\tau_p)^2 + \Theta^2}$. It also depends on the optical detuning ω' and the pump pulse duration τ_p, but does not depend on ϕ and θ. The Larmor frequency depends on the magnitude of the external magnetic field, but not on its direction.

As can be seen in Fig. S10c, S_b/S_a strongly depends on the spin coherence time T_2 due to efficiency of the spin amplification effect and on the pulse area Θ due to the Rabi frequency. The S_b/S_a value increases for spin systems with longer T_2. The dependence of the S_b/S_a value on T_2 reaches saturation with a value depending on the pump pulse area. Note that $\Theta = \pi$ is not optimal for the SML effect, despite that it is the optimal condition for spin coherence generation as explained in Ref. S22.

Figure S10d shows the range of T_2 and Θ for which the value of $S_b/S_a = 0.1$ is taken as in the experiment. It can be obtained for $\Theta \in [0.7\pi; 2\pi]$ with T_2 varying from 10 ns to 1 μs. There is an experimental way to estimate the

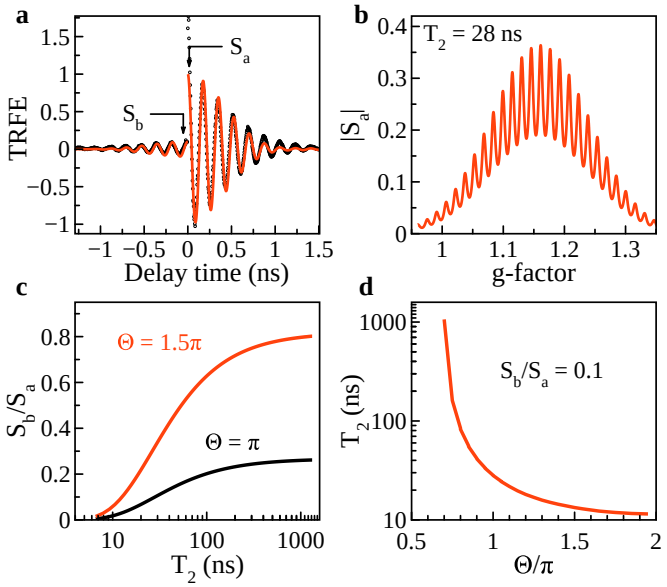

Supplementary Figure S10. **Modeling of spin dynamics without account for NIFF. a**, Time-resolved Faraday ellipticity signal (black dots) measured at $B_\mathrm{V} = 0.35$ T and its modeling (red line) using parameters: $T_\mathrm{R} = 13.2$ ns, $\Theta = \pi$, $\Delta\omega = 2.5$ rad/ns, $T_2 = 28$ ns, and $\omega' = 0$. **b**, Spectral distribution of precessing modes for $T_2 = 28$ ns. **c**, S_b/S_a dependence on T_2 for $\Theta = \pi$ (black line) and $\Theta = 1.5\pi$ (red line). **d**, Relation between the spin coherence time T_2 and the pulse power Θ for a fixed value of the amplitude ratio $S_b/S_a = 0.1$, as observed in the experiment.

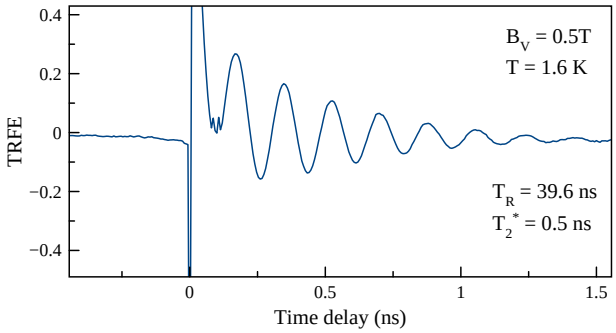

Supplementary Figure S11. **Time-resolved Faraday ellipticity measured at lower repetition rate.** Time-resolved Faraday ellipticity signal measured at $B_{\rm V} = 0.5\,{\rm T}$ and $T = 1.6\,{\rm K}$ for $T_{\rm R} = 39.6\,{\rm ns}$, pump power is 3.3 mW.

upper limit of T_2 time, namely to increase the period between laser pulses and reach the regime when spin coherence is fully decay before the next pump pulse arrival. In this case the SML signal amplitude at negative time delay should vanish. In Fig. S11 we show TRFE dynamics measured with a use of pulse-picker, which allows us to increase the laser repetition period up to $T_{\rm R} = 39.6$ ns. The SML signal is not detectable setting an upper limit for $T_2 < 40\,{\rm ns}$. For such rather short time the SML signal generation is possible only at high pumping intensities. For $\Theta = \pi$ the hole spin coherence time of $T_2 = 28$ ns can be evaluated.

S10: EVALUATION OF SPIN COHERENCE TIME IN THE PRESENCE OF NIFF

Determination of the spin coherence and spin dephasing times also requires an estimate of their value in the presence of nuclei-induced frequency focusing (NIFF). After the experimental observation of the NIFF effect in (In,Ga)As quantum dots, a number of models were proposed to describe it [S23–S28]. Among them, the model of dynamic nuclear polarization is the most physically transparent and universal one; it describes most of the observed experimental effects in various semiconductor structures [S29–S31]. This model considers nonresonant optical pumping of the hole or electron spin ensemble and dynamic nuclear polarization arising due to the transfer of the charge carrier spin to the ensemble of nuclei via the hyperfine interaction. Such flip-flop processes are most efficient in the presence of electron or hole spin component along the external magnetic field. It was noted in Ref. [S25] (see also [S20]) that corresponding spin component S_x along the magnetic field $\mathbf{B}_{\rm V} \parallel x$ can appear in our geometry taking into account the charge carrier spin rotation by the light pulse: In this case, there is an optical Stark field resulting in an effective magnetic field acting on the resident carrier spins that is directed along the wave vector of light. Due to the precession in this effective field, the spins gain a polarization projection (S_x) along the direction of the external magnetic field. The dynamics of nuclear polarization $I_{\rm N}$ along the magnetic field is described by the kinetic equation:

$$\frac{dI_{\rm N}}{dt} + \frac{1}{T_{1\rm h}}[I_{\rm N} - \bar{Q}\langle S_x(I_{\rm N})\rangle] + \frac{I_{\rm N}}{T_{\rm d}} = 0. \tag{S63}$$

Here $\bar{Q} = 4I(I+1)/3$ is a factor that depends on the nuclear spin I and $\bar{Q} = 1$ for perovskite NCs with $I(^{207}{\rm Pb}) = 1/2$, $\langle S_x(I_{\rm N})\rangle$ is the average spin polarization of the resident charge carrier along the magnetic field axis found from the solution of Eqs. (26-61), $T_{1\rm h}$ is the hyperfine coupling induced spin-flip time and $T_{\rm d}$ is the nuclear spin-lattice relaxation time, which takes into account any other possible spin-leakage mechanisms. $T_{\rm d} = 0.5\,{\rm s}$ is determined from experimental data shown in Fig. 2a in the main text. In the quasi-steady state conditions where the pulse train duration exceeds by far the nuclear relaxation times $dI_{\rm N}/dt$ can be neglected. The relative magnitude of these times can conveniently be summarized in the leakage factor $f_{\rm N} = T_{\rm d}/(T_{1\rm h} + T_{\rm d})$. The nuclear polarization produces a nonzero Overhauser field $B_{\rm N} = \alpha A_h I_{\rm N}/\mu_{\rm B} g_h$, which acts back on the carrier spins. For our case, the hyperfine constant for the hole spins with the ^{207}Pb isotope having a natural abundance of $\alpha = 0.22$ is $A_h = 33$ μeV Ref. [S1]. The nuclear polarization contributes to the total magnetic field $B_{\rm V} + B_{\rm N}$ providing the feedback on the hole spin precession with the effective

frequency $\omega_{\rm L} = \mu_{\rm B} g_h (B_{\rm V} + B_{\rm N})/\hbar$. Correspondingly, the hole-nuclear spin-flip rate can be estimated as

$$\frac{1}{T_{1\rm h}} \propto \left(\frac{A_h}{\hbar N}\right)^2 \frac{2F\tau_{\rm c}}{1+\omega_{\rm L}^2\tau_{\rm c}^2}, \tag{S64}$$

and depends on the nuclear polarization via $\omega_{\rm L}$. Here N is the number of unit cells within the hole orbit, for perovskite NCs $N = 10^4$ [S1], $\tau_{\rm c}$ is the correlation time in the hole-nuclear spin system, the factor F is the probability of finding the hole at the localization site. $\tau_{\rm c} = 13$ ns is the parameter chosen to fulfill the ratio of $\omega_{\rm L}\tau_{\rm c} \gg 1$ and $F = 1$ is taken as the fitting parameter. Details of the calculation and extended equations can be found in Ref. [S31].

The calculated Overhauser field distribution for perovskite NCs is shown in Fig. S12a in dependence on ω_x/ω_R. The Overhauser field is $B_{\rm N} = 0$ when ω_x is commensurate with $\omega_{\rm R}$ and is maximal for hole spins precessing with frequencies commensurate with $\omega_R/2$. Therefore, all precession frequencies lying between integer values $\omega_x/\omega_{\rm R}$ are dragged towards the precession modes. The nonlinearity in the system resulting from the dependence of the hole spin precession frequency on the nuclear polarization itself results in a variation of the nuclear spin-flip rates which, in turn, affects the build-up of the nuclear spin polarization.

As a result, a non-equilibrium distribution of nuclear fields is produced. An increase of the nuclear polarization results in suppression of nuclear spin fluctuations magnitude [S29, S32] and extension of the resident carrier spin dephasing time:

$$\mathcal{T}_2^* \propto \frac{\hbar}{\mu_B g_h \sqrt{\langle \delta B_{\rm N}^2 \rangle}}. \tag{S65}$$

One should note that suppression of the nuclear spin fluctuations lead to distribution of the spin coherence time around the mode position, therefore we define it by homogeneous dephasing time $\mathcal{T}_2^*$. In the main text and in the Supplementary Note S9, distribution of the spin coherence time around the mode position is not taken into account, so that the mode width is defined by T_2 and the width of the precession frequency distribution in the ensemble determines the inhomogeneous dephasing time T_2^*.

As suggested in Ref. [S29], for the carrier spins satisfying the PSC the strong feedback should lead to a reduction of the nuclear spin fluctuations. As soon as $\omega_x/\omega_{\rm R}$ differs from K, the nuclear fluctuations recover due to the reduced

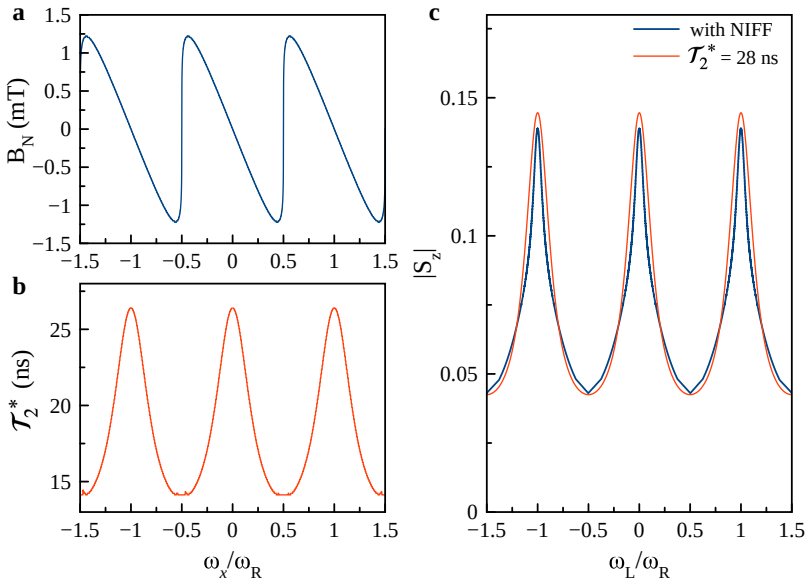

Supplementary Figure S12. **Nuclei-induced frequency focusing effect. a**, Calculated Overhauser field distribution as a function of $\omega_x/\omega_{\rm R}$ using the parameters $T_{\rm R} = 13.2$ ns, $\Theta = \pi$, $\mathcal{T}_{2,0}^* = 13$ ns, $I(^{207}{\rm Pb}) = 1/2$, $A_h = 33$ μeV, $\alpha = 0.22$, 10^4 nuclear spins, correlation time of the hole-nuclei spin interactions $\tau_c = 13$ ns, $T_d = 0.5$ s and $\omega'\tau_p/2\pi = 0.41$. **b**, $\mathcal{T}_2^*$ modulation in the presence of NIFF. **c**, Hole spin polarization distribution calculated for $\mathcal{T}_2^* = 28$ ns without NIFF (red line), and in the presence of NIFF for $\mathcal{T}_{2,0}^* = 13$ ns (blue line).

feedback strength. Therefore, depending on the magnetic field, the spin dephasing time becomes strongly modulated due to the periodic changes of the amplitude of the nuclear fluctuations.

We calculated the spin dephasing time $\mathcal{T}_2^*$ dependence on magnetic field with the parameters relevant for the studied $CsPb(Cl,Br)_3$ NCs and plotted it in Fig. S12b as a function of ω_x/ω_R. The modulation of $\mathcal{T}_2^*$ around the precession mode is clearly seen. Here we have used fitting parameter $\mathcal{T}_{2,0}^* = 13$ ns for the maximal nuclear spin fluctuations magnitude at $\omega_x/\omega_R = 1/2 + K$, where K is an integer. The suppression of nuclear spin fluctuations leads to a prolongation of the spin dephasing time of the hole spins precessing on $\omega_x/\omega_R = K$ as shown in Fig. S12b.

Figure S12c shows a calculated distribution near $\omega_x/\omega_R = 0$ and ± 1 to account for the spin dephasing time modulation in the dynamic nuclear polarization mechanism. The initial spin dephasing time is defined by the maximal magnitude of the nuclear spin fluctuations $\mathcal{T}_{2,0}^* = 13$ ns, which becomes then extended by the reduced nuclear fluctuation at the modes. Since the calculation is numerical, we cannot give an analytical equation for the peak width, but it is comparable to the peak width for the hole polarization calculated without the NIFF effect, or for constant $\mathcal{T}_2^* = T_2 = 28$ ns.

To summarize, the effect of suppression of nuclear spin fluctuations in the dynamic nuclear polarization mechanism leads to an effective prolongation of the spin coherence time on the precession modes. This means that for a constant ratio of the mode-locking amplitudes $S_b/S_a = 0.1$ the spin coherence time extracted from the model is shorter if the NIFF effect is taken into account, $\mathcal{T}_{2,0}^* = T_2 = 13$ ns, and longer if it is neglected, $T_2 = 28$ ns.

SUPPLEMENTARY REFERENCES

[S1] Kirstein, E., Yakovlev, D. R., Glazov, M. M., Evers, E., Zhukov, E. A., Belykh, V. V., Kopteva, N. E., Kudlacik, D., Nazarenko, O., Dirin, D. N., Kovalenko, M. V. and Bayer, M. Lead-dominated hyperfine interaction impacting the carrier spin dynamics in halide perovskites. *Advanced Materials* **34**, 2105263 (2022).

[S2] Ivchenko, E. L. *Optical Spectroscopy of Semiconductor Nanostructures* (Alpha Science, Harrow, UK, 2005).

[S3] Glazov, M. M. *Electron & Nuclear Spin Dynamics in Semiconductor Nanostructures* (Oxford University Press, Oxford, UK, 2018).

[S4] Grigoryev, P. S., Belykh, V. V., Yakovlev, D. R., Lhuillier, E. and Bayer M. Coherent spin dynamics of electrons and holes in $CsPbBr_3$ colloidal nanocrystals. *Nano Lett.* **21**, 8481–8487 (2021).

[S5] Canneson, D., Shornikova, E. V., Yakovlev, D. R., Rogge, T., Mitioglu, A. A., Ballottin, M. V., Christianen, P. C. M., Lhuillier, E., Bayer, M. and Biadala, L. Negatively charged and dark excitons in $CsPbBr_3$ perovskite nanocrystals revealed by high magnetic fields. *Nano Lett.* **17**, 6177–6183 (2017).

[S6] Efros, Al. L. in *Semiconductor and Metal Nanocrystals: Synthesis and Electronic and Optical Properties* (ed. Klimov, V. I.) Chapter 3, pp. 103–141 (Dekker, New York, 2003).

[S7] Kirstein, E., Yakovlev, D. R., Glazov, M. M., Zhukov, E. A., Kudlacik, D., Kalitukha, I. V., Sapega, V. F., Dimitriev, G. S., Semina, M. A., Nestoklon, M. O., Ivchenko, E. L., Kopteva, N. E., Dirin, D. N., Nazarenko, O., Kovalenko, M. V., Baumann, A., Höcker, J., Dyakonov, V. and Bayer, M. The Landé factors of electrons and holes in lead halide perovskites: universal dependence on the band gap. http://arxiv.org/abs/2112.15384, 31 December 2021.

[S8] Kalevich, V. K. and Korenev, V. L. Optical polarization of nuclei and ODNMR in GaAs/AlGaAs quantum wells. *Appl. Magn. Reson.* **2**, 397 (1991).

[S9] Yugova, I. A., Glazov, M. M., Yakovlev, D. R., Sokolova, A. A. and Bayer, M. Coherent spin dynamics of electrons and holes in semiconductor quantum wells and quantum dots under periodical optical excitation: Resonant spin amplification versus spin mode locking. *Phys. Rev. B* **85**, 125304 (2012).

[S10] Hernandez, F. G. G., Greilich, A., Brito, F., Wiemann, M., Yakovlev, D. R., Reuter, D., Wieck, A. D. and Bayer, M. Temperature-induced spin-coherence dissipation in quantum dots. *Phys. Rev. B* **78**, 041303 (2008).

[S11] Varwig, S., René, A., Greilich, A., Yakovlev, D. R., Reuter, D., Wieck, A. D. and Bayer, M. Temperature dependence of hole spin coherence in (In,Ga)As quantum dots measured by mode-locking and echo techniques. *Phys. Rev. B* **87**, 115307 (2013).

[S12] Varwig, S., Schwan, A., Barmscheid, D., Müller, C., Greilich, A., Yugova, I. A., Yakovlev, D. R., Reuter, D., Wieck, A. D. and Bayer, M. Hole spin precession in a (In,Ga)As quantum dot ensemble: From resonant spin amplification to spin mode locking. *Phys. Rev. B* **86**, 075321 (2012).

[S13] Greilich, A., Oulton, R., Zhukov, E. A., Yugova, I. A., Yakovlev, D. R., Bayer, M., Shabaev, A., Efros, Al. L., Merkulov, I. A., Stavarache, V., Reuter, D. and Wieck, A. Optical control of spin coherence in singly charged (In,Ga)As/GaAs quantum dots. *Phys. Rev. Lett.* **96**, 227401 (2006).

[S14] Heisterkamp, F., Zhukov, E. A., Greilich, A., Yakovlev, D. R., Korenev, V. L., Pawlis, A. and Bayer, M. Longitudinal and transverse spin dynamics of donor-bound electrons in fluorine-doped ZnSe: Spin inertia versus Hanle effect. *Phys. Rev. B* **91**, 235432 (2015).

[S15] Smirnov, D. S., Zhukov, E. A., Kirstein, E., Yakovlev, D. R., Reuter, D., Wieck, A. D., Bayer, M., Greilich, A. and Glazov, M. M. Theory of spin inertia in singly charged quantum dots. *Phys. Rev. B* **98**, 125306 (2018).

[S16] Mikhailov, A. V., Belykh, V. V., Yakovlev, D. R., Grigoryev, P. S., Reithmaier, J. P., Benyoucef, M. and Bayer, M.

Electron and hole spin relaxation in InP-based self-assembled quantum dots emitting at telecom wavelengths. *Phys. Rev. B* **98**, 205306 (2018).

[S17] Nestoklon, M. O. Tight-binding description of inorganic lead halide perovskites in cubic phase. *Computational Materials Science* **196**, 110535 (2021).

[S18] Bir, G. L. and Pikus, G. E. *Symmetry and Strain-Induced Effects in Semiconductors.* (Nauka, Moscow, 1972; Wiley, New York, 1975).

[S19] Landau, L. D. and Lifshitz, E. M. *Quantum Mechanics: Non-Relativistic Theory.* (Pergamon Press, Oxford, 2006).

[S20] Yugova, I. A., Glazov, M. M., Ivchenko, E. L. and Efros, Al. L. Pump-probe Faraday rotation and ellipticity in an ensemble of singly charged quantum dots. *Phys. Rev. B.* **80**, 104436 (2009).

[S21] Greilich, A., Shabaev, A., Yakovlev, D. R., Efros, Al. L., Yugova, I. A., Reuter, D., Wieck, A. D. and Bayer, M. Nuclei-induced frequency focusing of electron spin coherence. *Science* **317**, 1896–1899 (2007).

[S22] Yugova, I. A., Glazov, M. M., Yakovlev, D. R., Sokolova, A. A. and Bayer, M. Coherent spin dynamics of electrons and holes in semiconductor quantum wells and quantum dots under periodical optical excitation: Resonant spin amplification versus spin mode locking. *Phys. Rev. B* **85**, 125304 (2012).

[S23] Greilich, A., Shabaev, A., Yakovlev, D. R., Efros, Al. L., Yugova, I. A., Reuter, D., Wieck, A. D. and Bayer, M. Nuclei-induced frequency focusing of electron spin coherence. *Science* **317**, 1896–1899 (2007).

[S24] Carter, S. G., Shabaev, A., Economou, Sophia E., Kennedy, T. A., Bracker, A. S. and Reinecke, T. L. Directing nuclear spin flips in InAs quantum dots using detuned optical pulse trains. *Phys. Rev. Lett.* **102**, 167403 (2009).

[S25] Korenev V. L. Multiple stable states of a periodically driven electron spin in a quantum dot using circularly polarized light. *Phys. Rev. B* **83**, 235429 (2011).

[S26] Glazov, M. M., Yugova, I. A. and Efros, Al. L. Electron spin synchronization induced by optical nuclear magnetic resonance feedback. *Phys. Rev. B* **85**, 041303(R) (2012).

[S27] Beugeling, W., Uhrig, G. S. and Anders, F. B. Quantum model for mode locking in pulsed semiconductor quantum dots, *Phys. Rev. B* **94**, 245308 (2016).

[S28] Jäschke, N., Fischer, A., Evers, E., Belykh, V. V., Greilich, A, Bayer, M. and Anders, F. B. Nonequilibrium nuclear spin distribution function in quantum dots subject to periodic pulses. *Phys. Rev. B* **96**, 205419 (2017).

[S29] Zhukov, E. A., Kirstein, E., Kopteva, N. E., Heisterkamp, F., Yugova, I. A., Korenev, V. L., Yakovlev, D. R., Pawlis, A., Bayer, M. and Greilich, A. Discretization of the total magnetic field by the nuclear spin bath influorine-doped ZnSe. *Nat. Commun.* **9**, 1941 (2018).

[S30] Evers, E., Kopteva, N. E., Yugova, I. A., Yakovlev, D. R., Bayer, M. and Greilich, A. Suppression of nuclear spin fluctuations in an InGaAs quantum dot ensemble by GHz-pulsed optical excitation. *npj Quantum Information* **7**, 60 (2021).

[S31] Evers, E., Kopteva, N. E., Yugova, I. A., Yakovlev, D. R., Bayer, M. and Greilich, A. Shielding of external magnetic field by dynamic nuclear polarization in (In,Ga)As quantum dots. *Phys. Rev. B* **104**, 075302 (2021).

[S32] Smirnov, D. S. Spin noise of localized electrons interacting with optically cooled nuclei, *Phys. Rev. B* **91**, 205301 (2015).